buildings

MDPI

Article

Bond Transfer Mechanisms and Slip Evolution in High-Strength Concrete-Filled Steel Tubes Under Extreme Temperatures Through Push-Out Tests and Finite Element Simulations

Mingyong Zhong [1], Yingjun Yang [2,*], Wenfeng Zhou [3], Xingtao Liu [3], Xijuan Yang [1] and Li Wang [1]

[1] School of Civil Engineering, Lanzhou Jiaotong University, Lanzhou 730070, China
[2] Gansu Road & Bridge Construction Group Co., Ltd., Lanzhou 730070, China
[3] Gansu Wantai Construction Engineering Co., Ltd., Lanzhou 730070, China
* Correspondence: gslqjt@gslq.com

Abstract

The effects of wide-ranging service temperatures on interfacial bond transfer and slip evolution in high-strength concrete-filled steel tube members have not yet been systematically characterized. A test program involving 15 circular specimens was carried out at temperatures between −60 °C and 60 °C with steel tube wall thicknesses of 2 mm, 3 mm, and 4 mm. Particular attention was given to interface failure patterns, slip development, and stress transfer during loading. Cooling markedly enhanced the interfacial resistance, whereas heating produced a moderate reduction. The increase observed at subzero temperatures was smaller than that commonly reported for conventional concrete-filled steel tubes. Bond capacity also declined as the diameter-to-thickness ratio increased because of reduced confinement from the steel tube. Regression of the experimental data produced expressions for ultimate bond strength and the associated slip. A piecewise constitutive relation was then formulated to represent the complete bond–slip process. The proposed relation was implemented in ABAQUS through distributed nonlinear connector elements and temperature-dependent material properties. Numerical predictions showed close agreement with the measured load–slip responses, characteristic loads, and stress distributions. These results provide a modeling basis for HSCFST members exposed to severe cold and large temperature fluctuations.

Keywords: steel–concrete interface; temperature-dependent bond transfer; interfacial slip evolution; diameter-to-thickness ratio; piecewise constitutive modeling; nonlinear connector elements

Check for updates

Academic Editor: Vipul Patel

Received: 26 July 2026
Revised: 27 August 2026
Accepted: 27 August 2026
Published: 7 September 2026

Copyright: © 2026 by the authors. Licensee MDPI, Basel, Switzerland. This article is an open access article distributed under the terms and conditions of the Creative Commons Attribution (CC BY) license.

1. Introduction

High-strength concrete (HSC) with long durability, excellent construction performance, and significant economic and social benefits has become an essential material for meeting the demands of modern engineering constructions, such as super high-rise buildings and long-span bridges [1,2]. The brittleness of HSC gradually increases as its strength rises [3]. However, the brittleness of HSC cannot be adequately resolved merely by incorporating raw materials or admixtures; thus, researchers generally address this issue by encasing HSC in steel tubes, thereby harnessing its high-strength advantages. High-strength concrete-filled steel tubes (HSCFST), which are proven as high-performance composite members, provide excellent confinement to internal HSC to decrease its high brittleness. Consequently, the internal concrete effectively prevents the buckling of steel tubes, enabling the two

materials to complement each other and fully leverage their respective advantages [4,5]. Interfacial bond strength, which facilitates stress transfer between HSC and steel tubes in HSCFST columns, is essential for the two materials to work together. As the transportation network over the whole world continues to expand into regions with harsh climates, high seismic intensities, and large temperature differences, it is essential to study the mechanical properties of long-span bridges and high-rise buildings constructed with HSCFST at extreme service temperatures, and bonding performance becomes a critical parameter in such investigations [5–8].

China has a vast territory, covering multiple climatic zones and exhibiting significant regional variations in extreme temperatures. The extreme temperature data presented in Table 1 were obtained from the China Meteorological Data Network (https://data.cma.cn, accessed on 21 April 2026), which is operated by the National Meteorological Information Center of the China Meteorological Administration. The data were derived from historical surface meteorological observations recorded at representative meteorological stations. According to these records, the highest temperature in Xinjiang reached 52 °C, whereas the lowest temperature was −50 °C. In Mohe, Heilongjiang Province, the maximum and minimum recorded temperatures were 33 °C and −53 °C, respectively. These extreme conditions demonstrate that HSCFST structures inevitably experience various temperature loads in actual ambient conditions, leading to changes in their material properties due to temperature fluctuations. At subzero temperatures, free water in concrete may freeze and undergo volumetric expansion (approximately 9% upon ice formation), whereas steel undergoes thermal contraction and may exhibit increased brittleness. There are significant differences between the thermal conductivity (the thermal conductivity coefficient of steel is approximately 50 times higher than that of concrete), shrinkage creep, Poisson's ratio, and other properties of steel and concrete [9,10]. During heating and cooling cycles, the differences between the thermal conductivity and linear expansion coefficients of steel tubes and concrete result in a temperature difference, leading to a variation in interfacial stress. During heating, steel tubes rapidly conduct heat, and their radial expansion gets constrained by high temperatures, whereas the core concrete remains cooler. This temperature difference generates radial tensile stress at interfaces, potentially causing a separation between steel tubes and concrete. On the contrary, during cooling, the core concrete retains higher temperatures than the cooler steel tubes, and this deformation mismatch hinders the radial contraction of steel tubes and generates radial compressive stress at interfaces, leading to a separation between steel tubes and concrete and also facilitating sliding [11]. This deformation discrepancy during temperature variations can adversely affect the bonding performance at interfaces of steel tubes and concrete, ultimately compromising the structural integrity and load-bearing capacity of steel–concrete composites.

Table 1. Historical extreme maximum (T_{max}) and minimum (T_{min}) temperatures recorded at representative meteorological stations in China.

Region	T_{max}/°C	T_{min}/°C
Xinjiang	52	−50
Xizang	30	−47
Gansu	39	−36
Heilongjiang	33	−53
Chongqing	45	−13
Zhejiang	43	−9

A great number of experimental and numerical studies on the mechanical properties of ordinary concrete-filled steel tube (CFST) structures under normal temperature environments [12–15] and fire conditions [16–18] have been conducted worldwide in recent

years. Push-out tests under normal temperature conditions are carried out to identify key parameters affecting CFST strength, such as cross-section type, diameter–thickness ratio, inner surface roughness of steel tubes, and concrete age. Tao et al. [16] analyzed the post-fire bond behavior at the steel tube–concrete interface through finite element simulations and reported that the slip corresponding to the ultimate bond strength increased with increasing fire exposure duration. Song et al. [17] conducted 24 push-out tests to examine the bond strength of CFST columns at high temperatures and noticed that the interfacial bonds between steel tubes and concrete completely fractured during a fire. Based on experimental findings, researchers have proposed semi-analytical prediction models for interfacial bond strength between steel tubes and concrete. For example, Roeder and Xue et al. [13,19] developed calculation methods based on concrete strength, the diameter–thickness ratio, and cross-sectional dimensions. Yan [20] proposed a prediction formula for the ultimate bond strength of CFST columns at low temperatures. Kang, Liu, and Hu et al. [21–23] used finite element software, such as ANSYS and ABAQUS, to simulate bond–slip at interfaces of CFST columns under normal temperature conditions, analyzed the variation patterns of bond force and slip, revealed the force mechanism of bond slip, and proposed calculation methods for interfacial bond strength. More recently, Wang et al. [23] conducted push-out tests on 20 conventional CFST specimens under different ambient temperatures and investigated the effects of ambient temperature, diameter-to-thickness ratio, concrete strength, and specimen age on interfacial bond behavior. The study also examined the axial strain distribution of the steel tube and proposed an empirical expression for predicting the ultimate interfacial bond strength. This previous work provided an experimental basis for understanding temperature-dependent bond behavior in conventional CFST members. However, it focused primarily on conventional-strength CFSTs and on the prediction of ultimate bond strength, rather than on the complete evolution of the bond stress–slip response and its implementation in an interface constitutive model.

Despite these advances, the temperature-dependent interfacial behavior of HSCFST members remains insufficiently characterized. In particular, it is still unclear whether the temperature-dependent bond response observed in conventional CFST members can be directly extended to HSCFST members, because high-strength concrete differs from conventional concrete in strength, brittleness, pore structure, and water–cement ratio. Moreover, the complete evolution of the bond stress–slip response of HSCFST members under different ambient temperatures and its constitutive representation remain insufficiently investigated. Building on the previous study [24], the present work extends the investigation specifically to HSCFST members in three aspects. First, the temperature-dependent interfacial response of HSCFST members is examined to determine whether the behavior previously observed in conventional CFST members remains applicable when high-strength concrete is used. Second, the analysis is extended from the prediction of ultimate bond strength to the complete evolution of the bond stress–slip response, and a piecewise constitutive relationship is established based on the characteristic stages of the measured curves. Third, the proposed constitutive relationship is implemented in ABAQUS through distributed nonlinear connector elements to reproduce the global load–slip response and examine the associated stress-transfer behavior.

Accordingly, push-out tests were conducted on 15 circular HSCFST specimens at five ambient temperatures ranging from −60 °C to 60 °C and three steel-tube wall thicknesses. The experimental results were used to evaluate failure characteristics, slip evolution, and bond resistance, followed by the development of empirical bond parameters, a piecewise bond stress–slip constitutive relationship, and its finite element implementation.

2. Experimental Section

2.1. Specimen Design and Preparation

A total of 15 HSCFST short columns with a diameter of 140 mm were fabricated and subjected to push-out tests to investigate the effects of environmental temperature (T) and the diameter–thickness ratio (D/t) on the interfacial bonding performance of HSCFST structures. Considering the impacts of extremely high and low ambient temperatures, five different temperature conditions of 60, 20, 0, −20, and −60 °C were designed. Three different steel tube wall thicknesses (t) of 2, 3, and 4 mm were considered, and the series of specimens with a steel tube wall thickness of 3 mm served as the basic group. The inner steel tube surfaces were cleaned by manual descaling to achieve a rough surface condition without any oil contamination. The basic parameters of the specimens are presented in Table 2.

Table 2. Details of the tested specimens.

No.	Label	$D \times t \times L_i$/mm	T/°C	f_{cu}/MPa
1	C2-T60	140 × 2 × 420	60	69.5
2	C3-T60	140 × 3 × 420	60	69.5
3	C4-T60	140 × 4 × 420	60	69.5
4	C2-T20	140 × 2 × 420	20	82.9
5	C3-T20	140 × 3 × 420	20	82.9
6	C4-T20	140 × 4 × 420	20	82.9
7	C2-T0	140 × 2 × 420	0	87.6
8	C3-T0	140 × 3 × 420	0	87.6
9	C4-T0	140 × 4 × 420	0	87.6
10	C2-T(−20)	140 × 2 × 420	−20	92.1
11	C3-T(−20)	140 × 3 × 420	−20	92.1
12	C4-T(−20)	140 × 4 × 420	−20	92.1
13	C2-T(−60)	140 × 2 × 420	−60	108.6
14	C3-T(−60)	140 × 3 × 420	−60	108.6
15	C4-T(−60)	140 × 4 × 420	−60	108.6

Note: D is the outer steel tube diameter, Li is the bond length between the steel tube and the concrete, f_{cu} is the cube compressive strength of the concrete after 28 days of curing, Pu indicates the load at which bonding failure occurs, and S_u is the corresponding relative slip value. The specimen number C2-T60 denotes the specimen with a wall thickness of 2 mm and a service temperature of 60 °C.

All HSCFST specimens were made from the same cold-bent steel tubes. To minimize the influence of end effects on the test results, the ratio of the interfacial bond length to the steel tube diameter, L_i/D, was set to 3. With a steel tube diameter of 140 mm, the corresponding interfacial bond length L_i was therefore 420 mm. The total steel tube length L was set to 460 mm, leaving a 40 mm concrete-free region at the free end between the core concrete and the outer steel tube for the push-out tests. In addition, during specimen fabrication, longitudinal notches (10 mm × 40 mm) were machined at three different horizontal positions on each steel tube. Before setting the core concrete, steel bars (200 mm × 8 mm × 2 mm) were inserted horizontally through these longitudinal notches to measure the slip variation at different positions.

The three notches occupied only approximately 0.67–0.69% of the total bonded interface area, indicating that the interruption of the steel–concrete interface was highly localized. No apparent local buckling or abnormal deformation was observed around the notched regions during testing. Nevertheless, the notches may locally reduce the circumferential stiffness of the steel tube, and the inserted steel strips may introduce localized mechanical interaction with the concrete. Since unnotched control specimens were not

included in the present test program, these effects could not be quantitatively separated and should be regarded as a limitation of the experimental setup.

All push-out specimens and companion concrete cubes were cast from the same concrete batch and subjected to the same standard curing conditions at 20 ± 2 °C and a relative humidity of ≥95% for 28 days. After curing, the push-out specimens were conditioned to the prescribed target temperatures before testing. For the high-temperature conditions, the specimens were heated using electrical heating tapes uniformly wrapped around the steel tube surface. The temperature of the specimens was continuously monitored by PT100 sensors embedded in the core concrete. After reaching the prescribed target temperature, the specimens were maintained under this condition until the internal temperature became stable before the push-out tests were conducted.

2.2. Material Properties

The steel tubes used in this experiment were made of Q235 low-carbon steel. In order to obtain the material properties of the experimental steel, tensile test specimens were extracted from the steel tubes. According to GB/T 228.1-2021, GB/T 228.2-2015, and GB/T 228.3-2019 [25–27], tensile tests were conducted on steel specimens at room, elevated, and low temperatures, respectively (Figure 1). It is observable from the stress–strain curves of the steel samples shown in Figure 2 that both the yield strength and ultimate tensile strength of the experimental steel significantly increased as the temperature decreased, especially under low-temperature conditions. In addition, the ductility of the steel manifested a positive correlation with temperature. In low-temperature environments, reduced atomic thermal vibration enhanced interatomic bonding, suppressed dislocation motion and multiplication, and improved lattice stability, collectively enhancing the stiffness and strength of the material. The fundamental mechanical properties of the experimental steel, such as yield strength (f_y), ultimate tensile strength (f_u), Poisson's ratio (μ_s), and elongation (δ), are summarized in Table 3.



Figure 1. Tensile test of steel.

The mixing ratio of the core concrete, which was composed of P.O 42.5 ordinary Portland cement, granite coarse aggregate, sand, and water, is presented in Table 4. The strength of the concrete was measured by standard cubic compression tests in accordance with the GB/T50081-2019 Chinese standard (Standard for Test Methods of Physical and Mechanical Properties of Concrete) [28]. Three cubes of concrete with a side length of

150 mm were cast at each temperature, and concrete cube tests were conducted on the 28th day of standard curing (temperature 20 ± 2 °C, relative humidity ≥ 95%) and after being conditioned to the target temperatures (−60 °C, −20 °C, 0 °C, 20 °C, 60 °C) to obtain the failure patterns of the concrete at different temperatures (Figure 3). The compressive strengths of the concrete cubes are presented in Table 5.

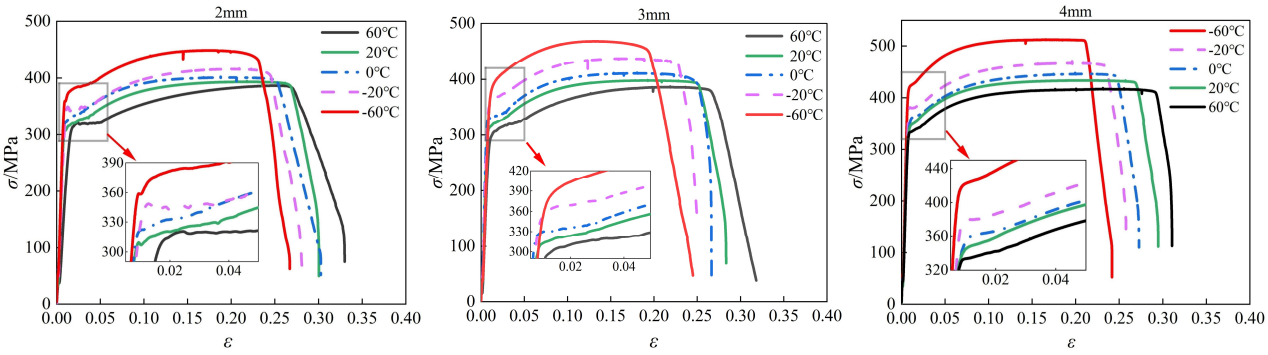


Figure 2. Stress-strain curves of steel at different temperatures.

Table 3. Mechanical properties of the Q235 steel.

t (mm)	T/°C	f_y/MPa	f_u/MPa	δ(%)	μ_s
2	60	320.31	386.36	28.19	0.290
	20	315.97	394.14	26.83	0.285
	0	321.33	401.28	25.76	0.278
	−20	349.25	417.73	24.83	0.274
	−60	385.85	450.50	18.36	0.263
3	60	308.32	385.46	29.27	0.293
	20	320.31	397.62	27.13	0.283
	0	341.98	412.88	26.54	0.279
	−20	369.53	447.83	25.44	0.276
	−60	396.43	471.48	19.81	0.268
4	60	332.10	421.88	29.89	0.298
	20	343.77	432.61	28.41	0.284
	0	356.43	451.37	27.56	0.281
	−20	379.53	472.65	26.38	0.275
	−60	420.01	511.90	20.14	0.271

Table 4. Concrete mix ratio (kg/m^3).

Fly Ash	Coarse Aggregate	Fine Aggregate	Water	Cement	Water Reducer	Air Entraining Admixture	Water Cement Ratio
120	931	850	131	359	6.23	2.39	0.36

As shown in Figure 3, the failure morphology of the concrete cubes varied noticeably with ambient temperature. At −60 °C, the specimen exhibited more pronounced fragmentation and spalling after reaching failure, indicating a relatively brittle failure mode. This observation is consistent with the substantially increased compressive strength measured at low temperature, where the concrete reached a higher failure load but experienced more abrupt damage after the peak resistance was attained. At 20 °C, the failure was mainly characterized by longitudinal cracking and localized spalling, while the overall specimen remained relatively intact. At 60 °C, multiple cracks and localized crushing were observed, accompanied by a reduction in compressive strength. These observations

indicate that ambient temperature affected not only the compressive strength but also the failure characteristics of the concrete.



(**a**) (**b**) (**c**)

Figure 3. Failure modes of concrete under different ambient temperatures: (**a**) low-temperature condition (−60 °C); (**b**) normal-temperature condition (20 °C); (**c**) high-temperature condition (60 °C).

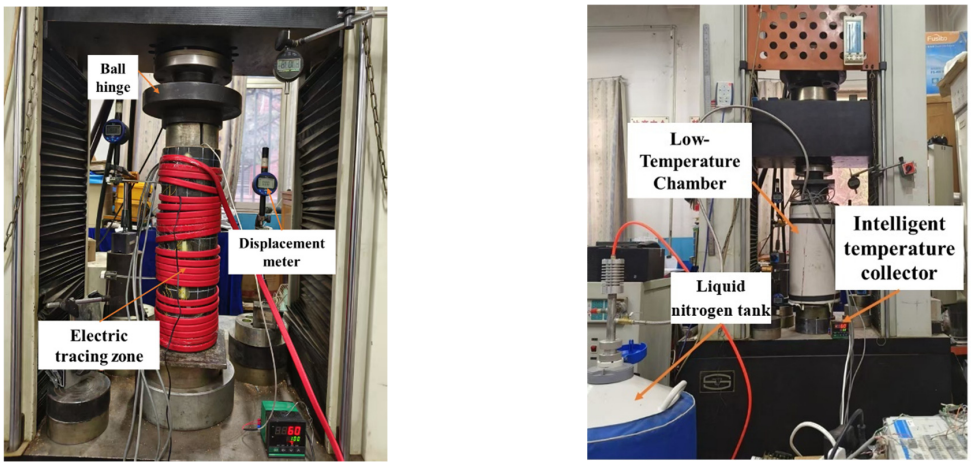
Table 5. Cube compressive strength of concrete.

T/°C	60	20	0	−20	−60
f_{cu}/MPa	69.5	82.9	87.6	92.1	108.6
f_c^T/MPa	43.6	52.0	54.9	57.8	68.1

2.3. Loading Device and Test Setup

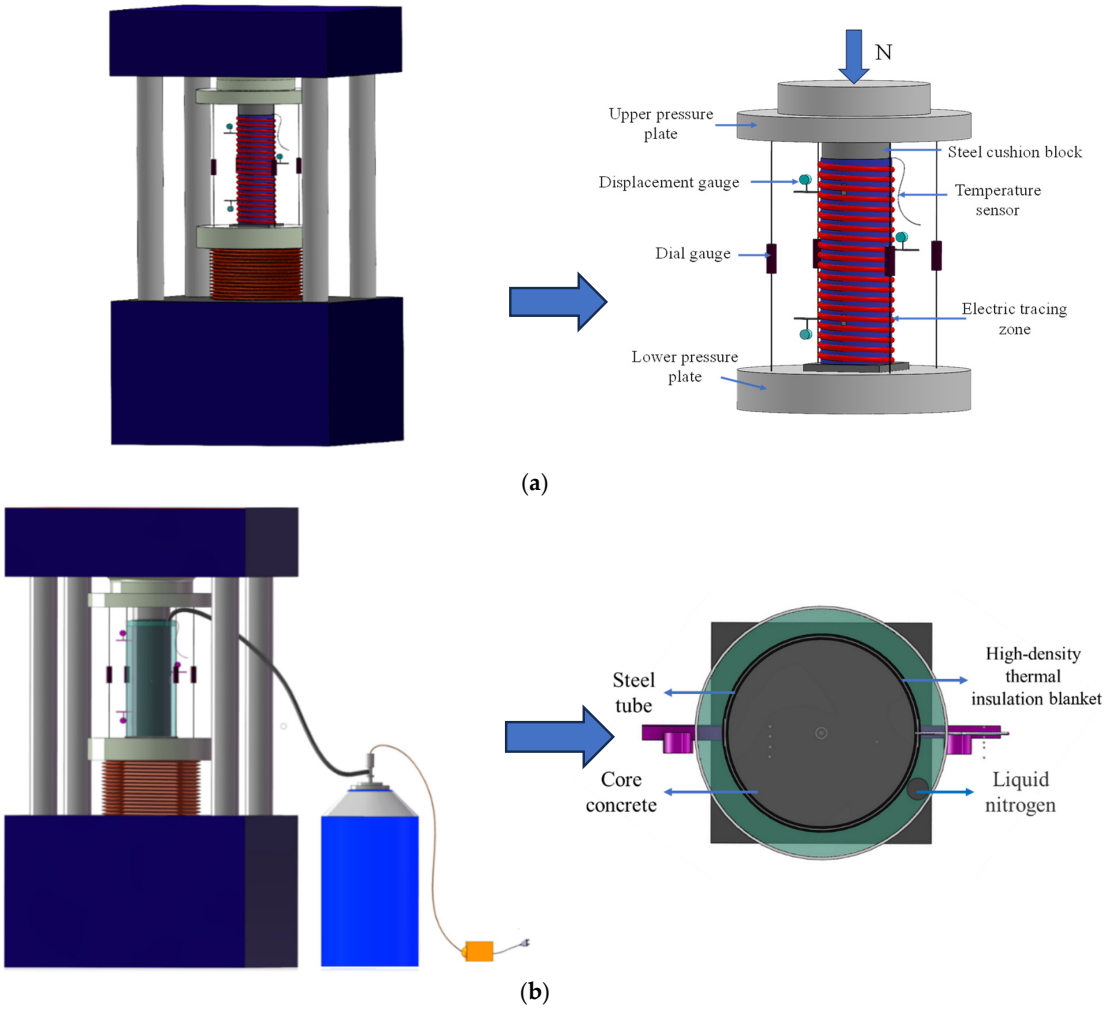
Push-out tests of the HSCFST columns were conducted on a 500 kN microcomputer-controlled electronic universal testing machine. The schematic diagrams of the temperature control device and the loading device are exhibited in Figures 4 and 5, respectively. A displacement gauge was vertically installed at the loading end to measure the relative slip of the core concrete. At various heights, a steel bar was inserted into the steel tube slot, with a displacement gauge attached through a magnetic base, to determine the interfacial slip between the steel tube and the concrete. Two rows of vertical strain gauges were symmetrically and evenly placed outside the steel tube on both sides of the unslotted section to measure longitudinal and circumferential strains during loading. To safeguard the strain gauges from damage and prevent them from falling off, they were encapsulated with epoxy resin. In this experiment, the most critical condition was to achieve and maintain the specimen target temperature in real time during the test. According to the GB51081-2015 Chinese standard [29], prior to conducting low-temperature tests, the specimens were placed in an ultra-low temperature chamber for 48 h to ensure that they reached the desired temperature. During the tests, an ambient temperature chamber was created around the specimens, and liquid nitrogen (LN_2) was injected to simulate a low-temperature ambiance, maintaining the target temperature. During high-temperature tests, the ambient temperature was achieved by wrapping self-limiting temperature electric heating tape around the exterior of the concrete columns, with a temperature control switch regulating the heating temperature. PT100 thermocouple sensors were placed inside the core concrete to monitor real-time temperatures during the push-out tests, and an LU-906M intelligent temperature acquisition instrument was used to record temperature variations. A total of 15 PT100 temperature sensors were used, with one sensor embedded at the geometric center of the core concrete for each specimen. The sensor locations were identical for all specimens to ensure consistent temperature measurement conditions. The temperature was maintained within ±2 °C of the target value throughout the test. Once the target temperature was achieved, staged loading was applied using load control, with each level set at 5% of the anticipated ultimate load and held for 1–2 min. Loading was continued

until nonlinear sliding occurred or 70% of the ultimate load was attained. Subsequently, displacement control ensured slow continuous loading until the core concrete at the free end achieved the desired position, with a maximum slip of 30 mm.



(**a**) (**b**)

Figure 4. Experimental setup for the temperature-controlled test: (**a**) high-temperature condition; (**b**) low-temperature condition.



(**a**)

(**b**)

Figure 5. Schematic diagram of the push-out test setup: (**a**) high-temperature loading device; (**b**) low-temperature loading device.

3. Experimental Results and Discussion

3.1. Failure Mode

During the push-out process, no significant buckling occurred on the outer surface of any of the steel tubes. Figure 6a–c displays the failure patterns of the core concrete at the loading end of the HSCFST columns under different temperature conditions. The edges of the core concrete in the low-temperature specimens exhibited more severe fragmentation, and it can be ascribed to the higher bond strength at the steel–concrete interface under low-temperature conditions, resulting in greater axial loads. Figure 6d–f illustrates the failure modes and interior conditions of the HSCFST columns after the push-out test. A significant number of longitudinal scratches was clearly observed at the steel tube–concrete interface due to the relative slip between the core concrete and the steel tube during the push-out process. In addition, after cutting open the external wall of the low-temperature specimens, a considerable amount of moisture was detected on the surfaces of the steel tube and the concrete; this is mainly because, under low-temperature conditions, the residual moisture observed at the steel tube–concrete interface after testing suggests that pore water may have frozen at the interface during cooling. Such ice formation may have provided additional interfacial resistance, contributing to the increased bond strength observed at subzero temperatures. After the completion of the test, the ice melted into water, leaving residual moisture at the steel tube–concrete interface. However, direct evidence of ice formation (e.g., imaging at sub-zero temperatures) was not obtained in this study, and the interpretation remains tentative. In the high-temperature HSCFST columns, localized areas exhibited a brownish discoloration, differing from that of the ambient-temperature specimens, and this phenomenon might be a result of partial debonding under high-temperature conditions.

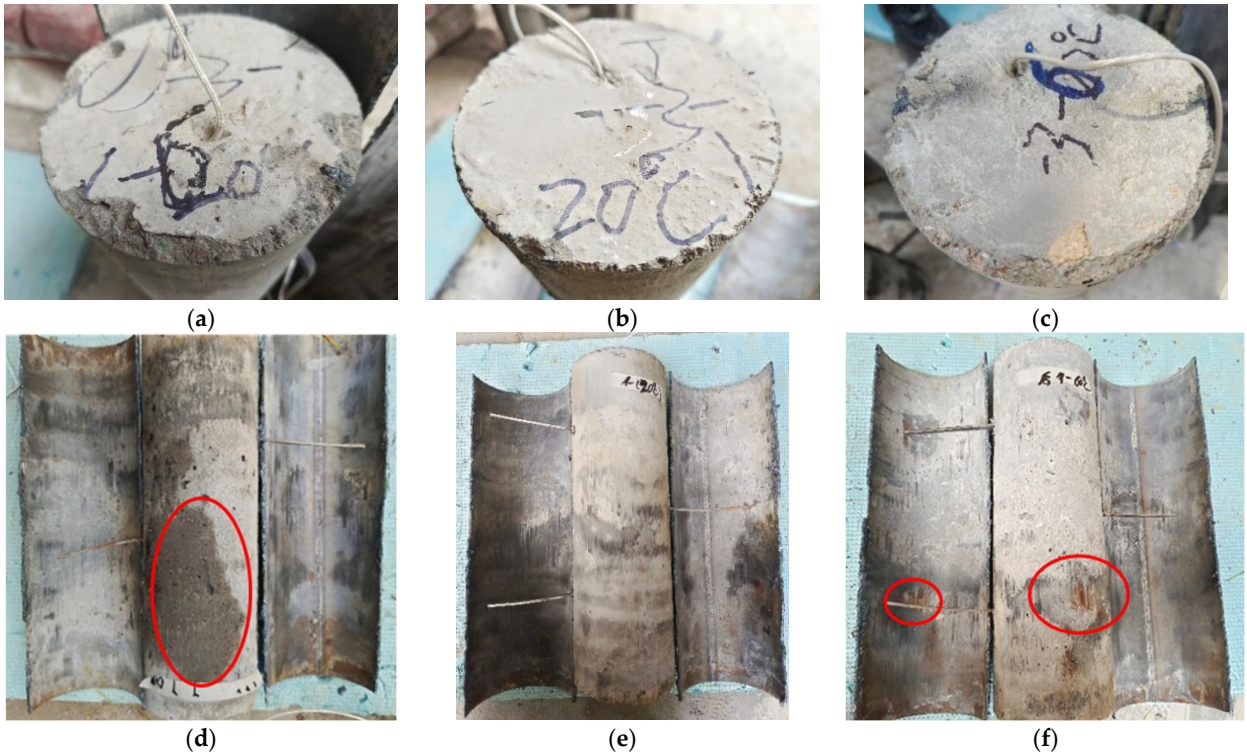


Figure 6. Failure modes of the HSCFST contact interface under different ambient temperatures: (**a**–**c**) damage morphology of core concrete at the loaded end under low-temperature (−60 °C), normal-temperature (20 °C), and high-temperature (60 °C) conditions, respectively; (**d**–**f**) cutting morphology of the external steel tube after the test under low-temperature (−60 °C), normal-temperature (20 °C), and high-temperature (60 °C) conditions, respectively. (red circles indicate the residual moisture and longitudinal scratches observed at the steel tube–concrete interface).

3.2. Bond Stress–Slip Curves

Previous studies have indicated that the local bond response at the steel–concrete interface may vary along the bonded length of CFST members [30–33]. In the present push-out tests, only the global load and relative slips at selected positions were measured; therefore, the local bond-stress distribution along the entire interface could not be directly determined. For this reason, an equivalent average bond stress (τ_u) was adopted to characterize the overall interfacial bond resistance of the HSCFST specimens, which can be calculated using Equation (1), and the calculation results are presented in Table 6.

$$\tau_u = \frac{P_u}{\pi D_0 l} \tag{1}$$

where P_u is the characteristic bond-damage load corresponding to point A, S_u is the associated slip, D_0 is the inner diameter of the steel tube, and l is the steel–concrete bond length. For curves exhibiting a distinct peak (Types II and III), P_u was taken as the load at the first peak. For peak-free curves (Type I), P_u was defined as the load at the first characteristic turning point, where the tangent stiffness decreased markedly from the initial ascending branch. The corresponding slip was taken as S_u; D_0 is the inner steel tube diameter, and l is the length of the steel tube–concrete interface.

Table 6. Detailed data of the push-out tests.

No.	Label	$D \times t \times L_i$/mm	T/°C	P_u/kN	τ_u/MPa	S_u/mm	Curve Type
1	C2-T60	140 × 2 × 420	60	101.26	0.564	2.739	Type II
2	C3-T60	140 × 3 × 420	60	103.81	0.587	3.271	Type II
3	C4-T60	140 × 4 × 420	60	147.26	0.845	3.884	Type I
4	C2-T20	140 × 2 × 420	20	106.94	0.596	5.228	Type II
5	C3-T20	140 × 3 × 420	20	108.91	0.616	3.367	Type III
6	C4-T20	140 × 4 × 420	20	168.06	0.965	3.149	Type I
7	C2-T0	140 × 2 × 420	0	112.33	0.626	3.805	Type III
8	C3-T0	140 × 3 × 420	0	126.83	0.717	4.207	Type III
9	C4-T0	140 × 4 × 420	0	184.09	1.057	4.294	Type I
10	C2-T(−20)	140 × 2 × 420	−20	144.30	0.804	4.168	Type II
11	C3-T(−20)	140 × 3 × 420	−20	145.98	0.826	4.258	Type II
12	C4-T(−20)	140 × 4 × 420	−20	188.95	1.085	5.126	Type II
13	C2-T(−60)	140 × 2 × 420	−60	180.85	1.008	2.330	Type II
14	C3-T(−60)	140 × 3 × 420	−60	198.61	1.123	3.571	Type I
15	C4-T(−60)	140 × 4 × 420	−60	251.90	1.446	4.859	Type II

Figure 7 displays the bond stress–slip (τ_u-S) curves of the HSCFST specimens with different wall thicknesses at different ambient temperatures. It is evident that the bond strength of HSCFST was negatively correlated with ambient temperature. For example, in the baseline group with a specimen thickness of 3 mm, when the temperature was increased to 60 °C, the bond strength of the C3-T60 interface decreased by 4.71% compared with that of the C3-T20 interface, and it can be attributed to the continuous dissipation of free water within the concrete at high temperatures, leading to an increase in pore volume within the concrete and exacerbating the loss of interfacial cement paste and chemical bonding forces. In contrast, when the ambient temperature was dropped to −60 °C, the bond strength of the C3-T(−60) interface increased by 82.31% compared with that of the C3-T20 interface. The improvement in the bond strength of HSCFST at low temperatures was found to be relatively smaller than that of ordinary CFST [33], and the reason for this was that, at low temperatures, the water–cement ratio significantly influenced both the

concrete strength and the bond strength at the steel tube–concrete interface. Lower-strength concrete structures generally have a higher water–cement ratio, which results in greater porosity and more water content. When the water freezes, it fills the internal voids of the concrete and adheres to the steel tube–concrete interface, causing additional adhesion stress and enhancing the inner surface roughness [34,35].

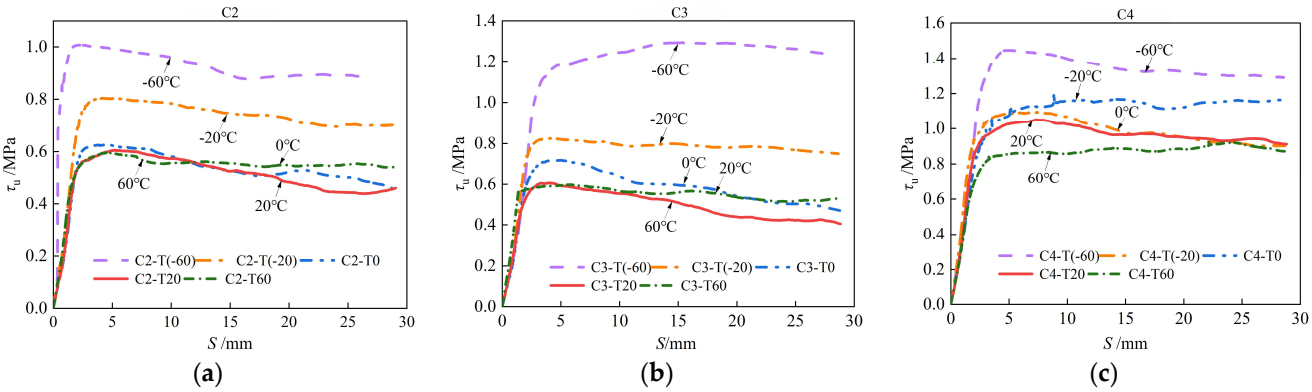


Figure 7. Effect of ambient temperature on the interfacial bond strength with different steel tube thicknesses: (**a**) 2 mm; (**b**) 3 mm; (**c**) 4 mm.

The moisture content of the push-out specimens was not directly measured before thermal conditioning. Therefore, the present study cannot quantitatively relate the measured bond enhancement to the initial moisture content of the concrete. However, all specimens were fabricated from the same concrete batch and subjected to an identical curing protocol, thereby minimizing differences in moisture condition among specimens before temperature conditioning.

Figure 8 presents the τ_u-S curves of the HSCFST specimens with different diameter–thickness ratios (D/t) at different ambient temperatures, and it is noticeable that the interfacial bond strength of HSCFST gradually decreased with the increase in the D/t value. For example, at 60 °C, as D/t increased from 35 to 46.67 and 70, the bond strength decreased from 0.845 MPa for C4-T60 to 0.587 MPa for C3-T60 and further to 0.564 MPa for C2-T60. Accordingly, the bond strength of C3-T60 was 30.53% lower than that of C4-T60 and 4.08% higher than that of C2-T60. Similarly, at −60 °C, C3-T(−60) exhibited a bond strength 22.34% lower than C4-T(−60) and 11.41% higher than C2-T(−60). These results confirm the overall decrease in bond strength with increasing D/t within the tested range. With the increase in D/t, the relative wall thickness of the steel tube decreased, thereby reducing its radial stiffness and confinement effect on the core concrete. The observed variation in circumferential strain further supports this explanation, because thicker steel tubes provide greater resistance against radial deformation. Consequently, the intensities of the radial confinement force and the normal force acting on the steel tube–concrete interface were reduced; thereby, both the confining effect and the interfacial bond strength were weakened [13,16].

3.3. Distribution of Longitudinal and Circumferential Strains Along the Height of Steel Tubes in HSCFST Columns

Figure 9 shows the strain gauge arrangement and longitudinal strain distribution of the basic group of HSCFSTs at different ambient temperatures and loading levels, where the vertical axis represents the distance from the loading end of the specimen. The longitudinal strain distribution on the external surface of the steel tube along the height of the HSCFST column varied with temperature. When the applied load reached 80% of the ultimate failure load, the longitudinal strain distribution on the outer wall

of the HSCFST column exhibited a roughly "V" shape (Figure 9b). When the maximum stress was attained, tensile stress was generated in the opposite direction, indicating that at higher ambient temperatures, local debonding occurred at the steel tube–concrete interface of HSCFST. In contrast, at lower temperatures, the required axial load increased as temperature decreased, and this can be attributed to fact that under sub-zero conditions, both the steel tube and the concrete undergo thermal contraction. However, the coefficient of thermal contraction differs significantly between the two materials, with steel contracting more than concrete. This differential contraction, combined with the volumetric expansion of freezing water (approximately 9% upon ice formation) within the concrete pores, creates complex interfacial stress states. The restraining effect of the steel tube on the concrete column prevented the free expansion and contraction of the concrete and increased the intensity of the interaction force between the steel tube and the concrete, causing an improvement in strain values on the external surface of the steel tube. It is observable from Figure 9f that when the ambient temperature was −60 °C, tensile stress appeared at the loading end of the external surface of the steel tube, then changed to compressive stress, and finally, reverted to tensile stress at the free end. This occurred because, when the load was applied to the loading end at the beginning of the test, the steel tube and the concrete experienced different degrees of shrinkage due to the temperature drop. The concrete experienced relatively less shrinkage, whereas the steel tube underwent greater shrinkage. Hence, during the initial loading stage, the steel tube was restrained by the concrete, and tensile stress was generated at the loading end of the external surface of the steel tube. As the load continued to increase, the interaction between the steel tube and the concrete was further improved. Under compressive conditions, the concrete tended to expand, whereas the steel tube restricted this deformation with its high strength and stiffness. Subsequently, the reaction force of the concrete on the steel tube caused the tensile stress at the loading end to gradually transform into compressive stress. When the force at the loading end was transmitted to the steel tube at the free end through the concrete, the 40-mm-long empty steel tube section at the free end lacked the support of the core concrete. At the low temperature of −60 °C, the shrinkage characteristics of the steel tube and the concrete became more pronounced. The shrinkage of the empty steel tube section was greater than that of the section wrapped with the concrete. Moreover, as no reaction force was generated from the concrete to balance the stress at the free end, tensile stress was more likely to appear there.

In addition to the longitudinal strain, the circumferential strain of the steel tube was analyzed to further characterize the radial interaction between the steel tube and the core concrete. Since the confinement effect in HSCFST members is primarily associated with the radial restraint provided by the steel tube, the circumferential deformation can provide direct evidence of the temperature-dependent interface interaction.

As shown in Figure 10, the circumferential strain increased with increasing load level under all temperature conditions, indicating that radial interaction between the steel tube and concrete was gradually mobilized during loading.

Compared with the specimens tested at higher temperatures, the specimens at −60 °C exhibited larger circumferential deformation. This phenomenon may be related to the combined effects of differential thermal contraction between steel and concrete and the possible expansion of frozen pore water. These effects increase the restraint demand imposed by the steel tube and enhance the radial interaction at the interface.

3.4. Load–Slip Curves of HSCFST at Different Interfaces

During the push-out test, relative slip values at different interfaces between the steel tube and the core concrete were measured. Three slots were opened in the steel tube wall,

and the relative slip values at different steel–concrete interfaces were measured by setting up displacement gauges in these slots (Figure 11).

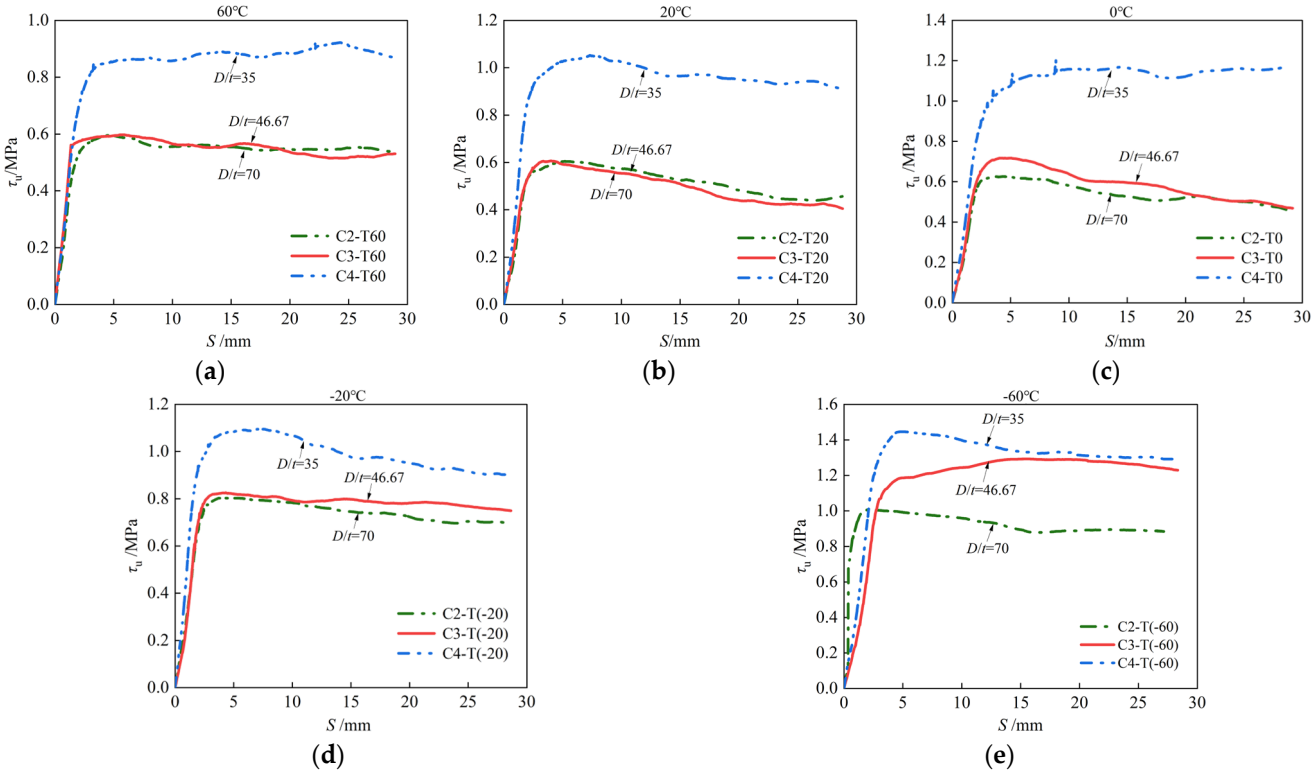


Figure 8. Effect of the diameter-to-thickness ratio (D/t) on the interfacial bond strength under different ambient temperatures: (**a**) 60 °C; (**b**) 20 °C; (**c**) 0 °C; (**d**) −20 °C; (**e**) −60 °C.

Figure 12 illustrates the load–slip curves of HSCFST for the basic group at different interfaces under the influence of various ambient temperatures. It is evident that the load value and the bond strength both varied at different positions. As the temperature decreased, the required axial load increased, and the slip values at the three groove positions exhibited greater variation before reaching the ultimate bond slip (S_u). The slip value at S3 was greater than those at S1 and S2 at high ambient temperatures (Figure 12a), and this happened because, at high temperatures, the different thermal expansion coefficients of the steel tube and the concrete led to nonuniform expansion between the two materials. The elevated temperature reduced the strength and elastic modulus of the concrete, making it more prone to deformation. In addition, the empty steel tube at S3 near the free end experienced relatively less resistance from the concrete, resulting in a larger slip value near the free end due to thermal expansion. Under sub-zero temperature conditions, both the steel tube and the concrete underwent shrinkage; however, their shrinkage degrees differed greatly (Figure 12c–e). As the steel tube had a higher shrinkage coefficient than the concrete, it contracted relatively faster during cooling. In the middle section, the differential shrinkage between the two materials generated significant stress due to the constraints at both ends, leading to a "necking effect" that induced relative slip at the interface [36]. Furthermore, in the sub-zero environments, moisture within the concrete migrated and potentially formed localized hydrostatic or frost-heave pressures in the middle section. These additional forces interacted with the bond strength and affected the interfacial stability, resulting in a larger slip value.

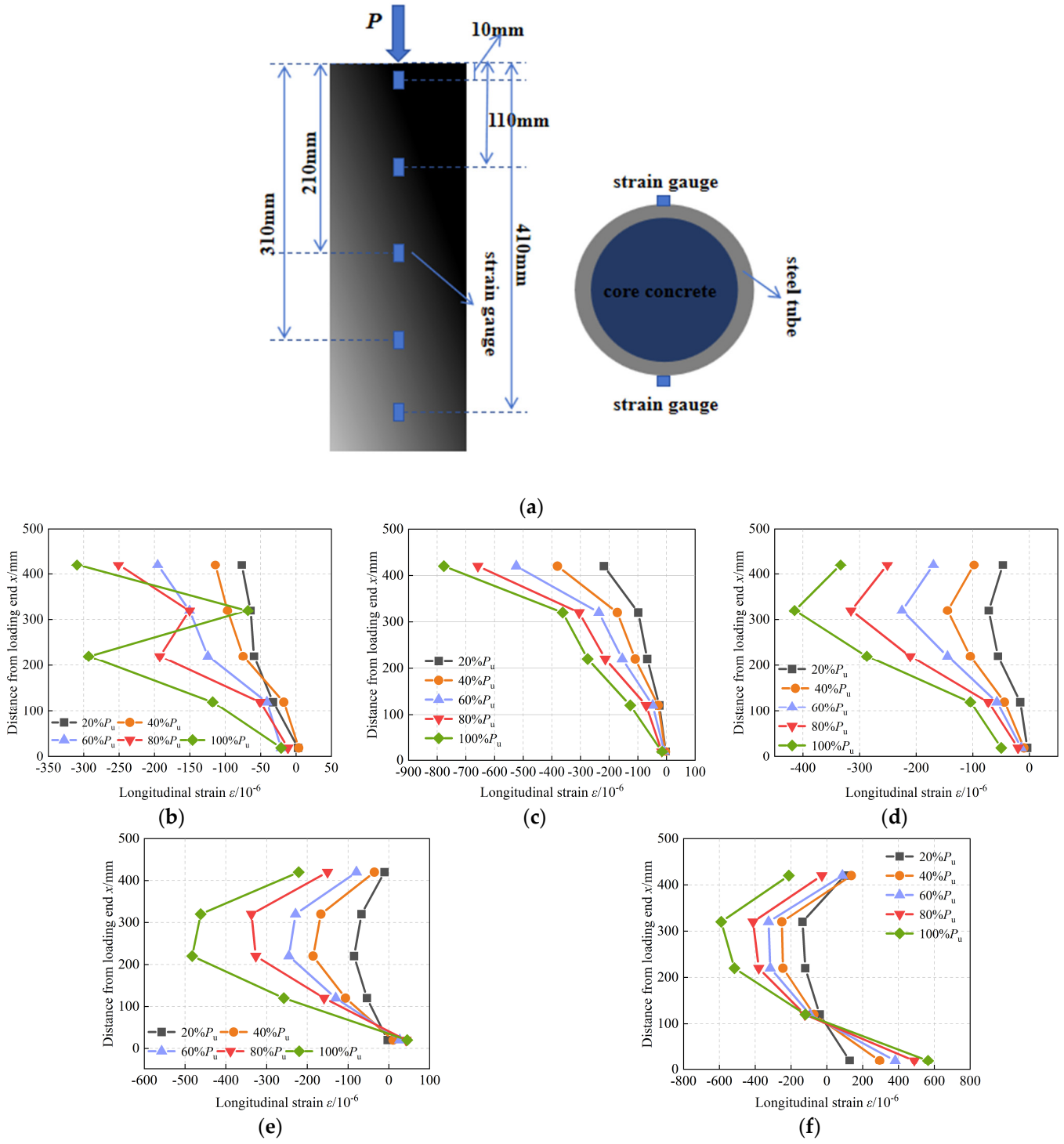


Figure 9. Strain gauge arrangement and longitudinal strain distribution on the outer surface of the steel tube under different ambient temperatures: (**a**) schematic diagram of strain gauge arrangement; (**b**–**f**) longitudinal strain distribution along the column height at 60 °C, 20 °C, 0 °C, −20 °C, and −60 °C, respectively.

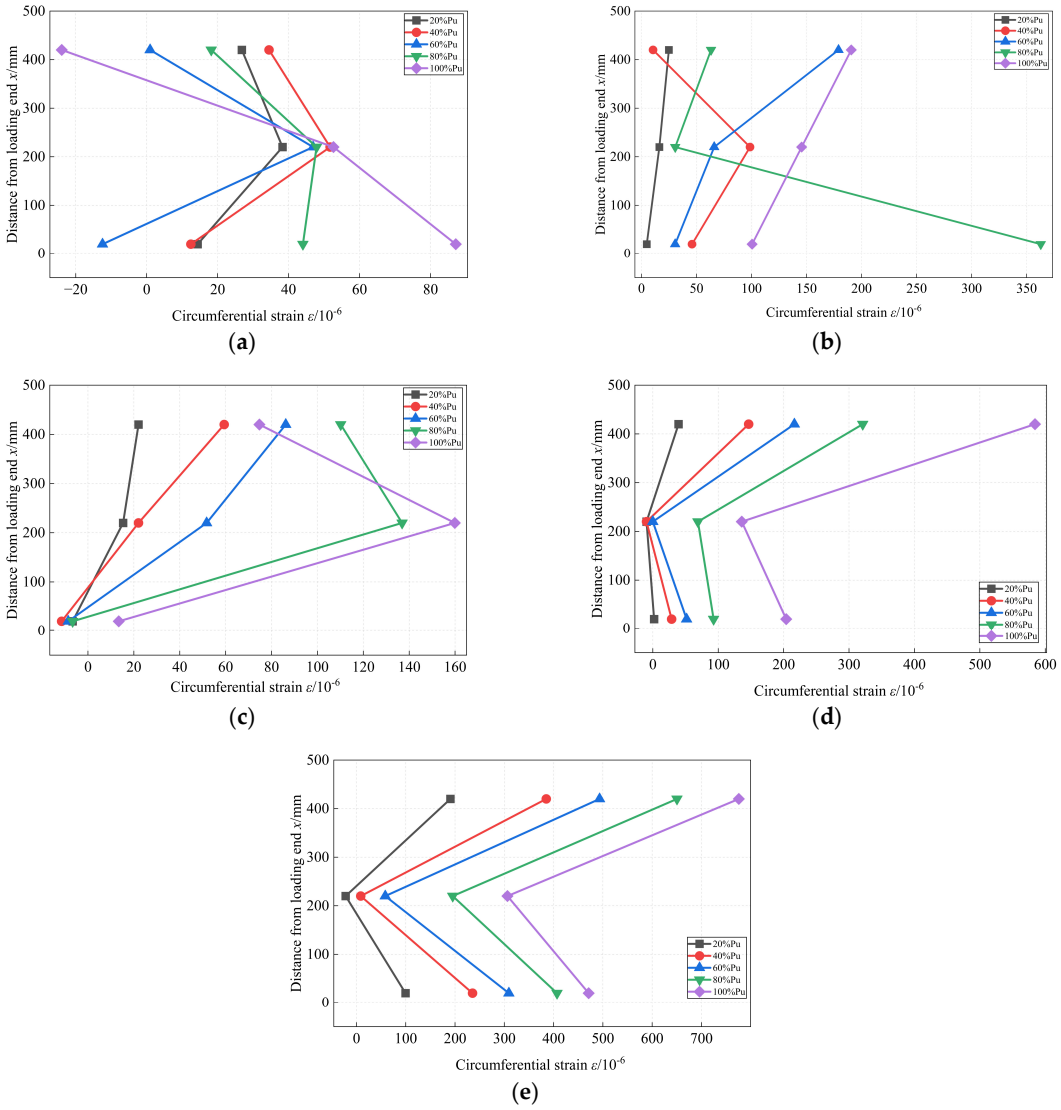


Figure 10. Circumferential strain distribution on the external surface of steel tubes under different ambient temperatures: (**a**) 60 °C; (**b**) 20 °C; (**c**) 0 °C; (**d**) −20 °C; (**e**) −60 °C.

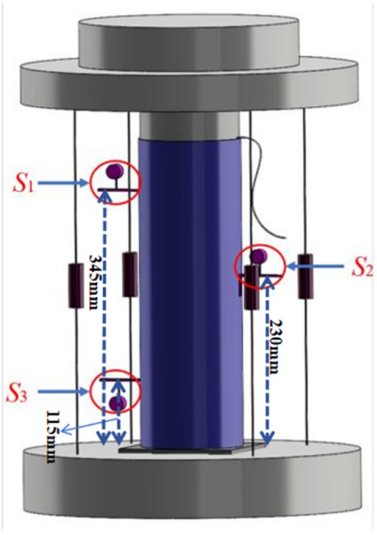


Figure 11. Schematic of the HSCFST external wall grooves at different interfaces.

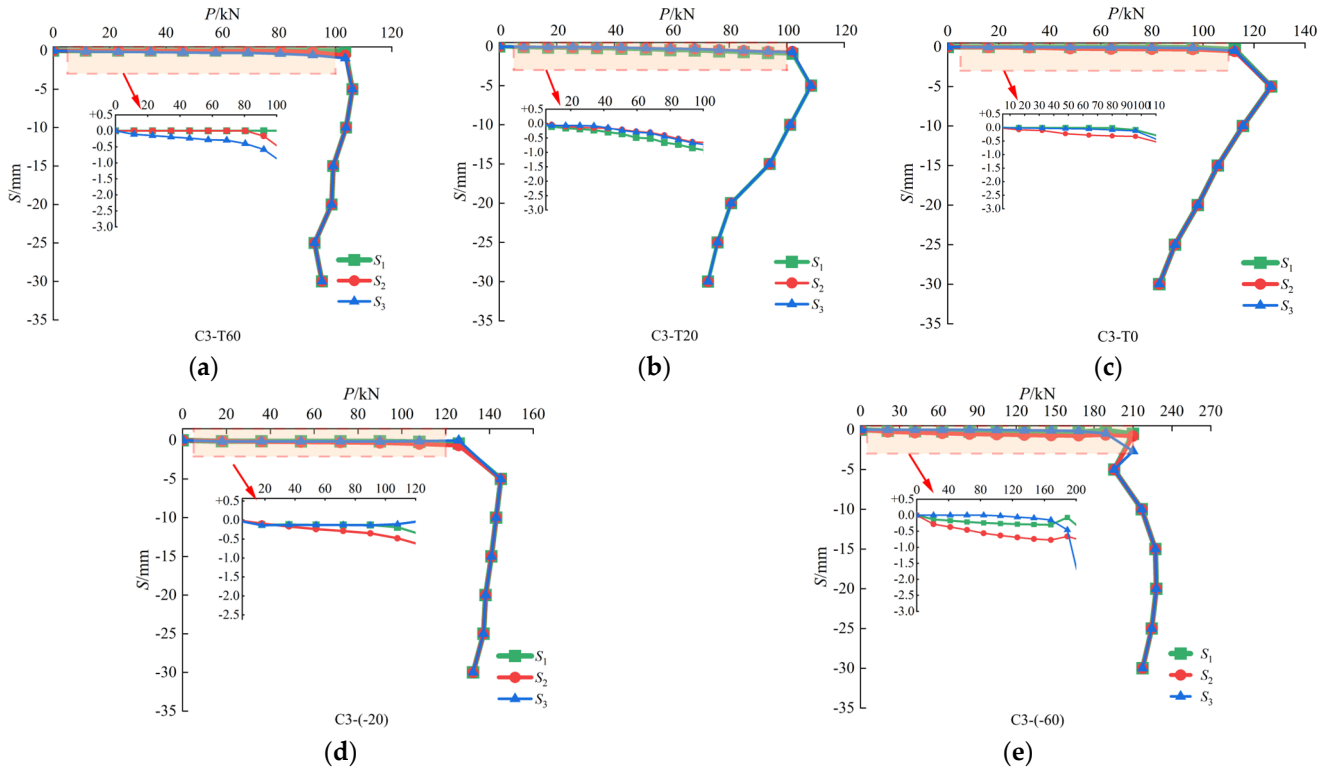


Figure 12. Load-slip curves at different interfaces of HSCFST specimens under different ambient temperatures: (**a**) 60 °C; (**b**) 20 °C; (**c**) 0 °C; (**d**) −20 °C; (**e**) −60 °C.

4. Bond Stress–Slip Constitutive Relationship of HSCFST Under the Influence of Ambient Temperature

4.1. Factors Affecting the Bond Strength of HSCFST

In order to evaluate the bonding performance of HSCFST at the steel tube–concrete interface under the influence of different ambient temperatures and D/t values, the interfacial bonding performance was analyzed using the ultimate bond strength (τ_u) as a criterion, and the τu values of the specimens are presented in Table 6.

4.1.1. Influence of Ambient Temperature (T) on Interfacial Bond Strength

The influence mechanism of different ambient temperatures on the interfacial bond strength of HSCFST is analyzed in Section 3.2, and it was found that the interfacial bond strength of HSCFST decreased linearly with the rise in ambient temperature. Figure 13a presents the relationship between ambient temperature and interfacial bond strength for the HSCFST specimens with the same concrete strength grade and different steel tube wall thicknesses of 2, 3, and 4 mm. The correlation formula between the ultimate bond strength and ambient temperature for the HSCFST specimens was obtained through statistical regression analysis.

$$\tau_u = -0.0039T + 0.7196 \ (t = 2 \text{ mm}), \quad (2)$$

$$\tau_u = -0.0045T + 0.7738 \ (t = 3 \text{ mm}), \quad (3)$$

$$\tau_u = -0.0048T + 1.0796 \ (t = 4 \text{ mm}), \quad (4)$$

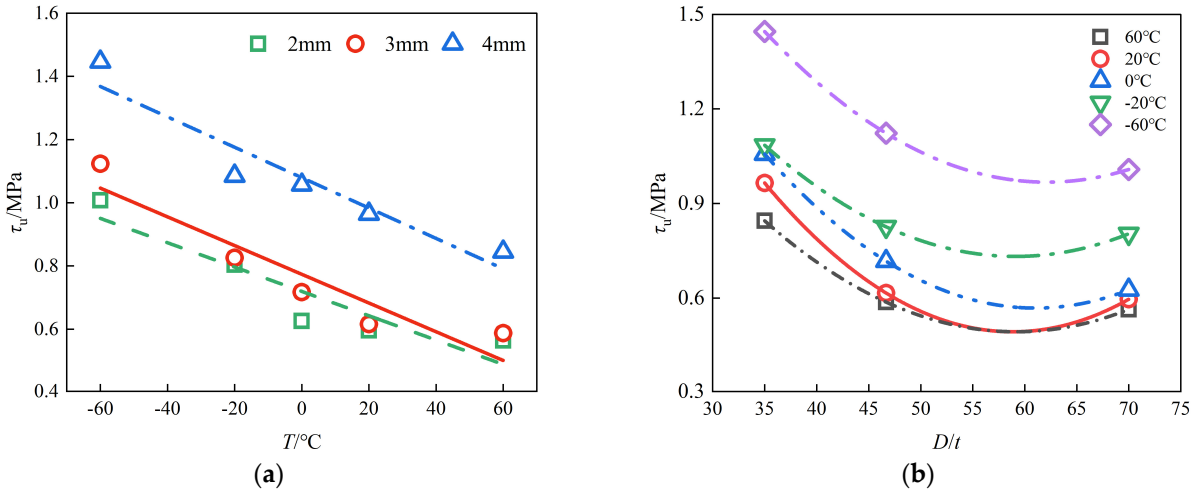


Figure 13. Effects of different parameters on the interfacial bond strength: (**a**) effect of ambient temperature; (**b**) effect of diameter-to-thickness ratio (D/t).

4.1.2. Influence of the Diameter–Thickness Ratio on Interfacial Bond Strength

The influence of D/t on the interfacial bond strength of HSCFST is discussed in Section 3.2. Within the tested range, the experimental results show an overall decrease in bond strength with increasing D/t. Because only three D/t levels (35, 46.67, and 70) were tested at each temperature, quadratic expressions were adopted only as interpolation relationships to describe the variation among the measured data points, rather than as validated functional laws. The corresponding interpolation expressions at different ambient temperatures for HSCFST short columns with (L/D = 3) are given in Equations (5)–(9).

$$\tau_u = 0.0006\left(\frac{D}{t}\right)^2 - 0.0714\frac{D}{t} + 2.605 \quad (T = 60\ ^\circ\mathrm{C}), \tag{5}$$

$$\tau_u = 0.0008\left(\frac{D}{t}\right)^2 - 0.0977\frac{D}{t} + 3.368 \quad (T = 20\ ^\circ\mathrm{C}), \tag{6}$$

$$\tau_u = 0.0007\left(\frac{D}{t}\right)^2 - 0.088\frac{D}{t} + 3.255 \quad (T = 0\ ^\circ\mathrm{C}), \tag{7}$$

$$\tau_u = 0.0006\left(\frac{D}{t}\right)^2 - 0.0718\frac{D}{t} + 2.854 \quad (T = -20\ ^\circ\mathrm{C}), \tag{8}$$

$$\tau_u = 0.0007\left(\frac{D}{t}\right)^2 - 0.0808\frac{D}{t} + 3.477 \quad (T = -60\ ^\circ\mathrm{C}), \tag{9}$$

4.2. Calculation and Validation of Interfacial Bond Parameters for HSCFST

4.2.1. Bond Strength and Bond Slip Calculation for HSCFST

The primary determinants for the interfacial bond strength of HSCFST were identified through statistical regression analysis, and significant relationships among bond strength, ambient temperature (T), and the diameter–thickness ratio (D/t) were detected. Figure 14 illustrates the impact of ambient temperature on concrete strength, and concrete strength under varying ambient temperatures was found as a critical factor affecting the interfacial bond performance [20,33]. The influences of three main factors—T, D/t, and f_{cu}—on interfacial bond strength were quantified through regression analysis, and as the impacts of other factors could not be quantitatively analyzed, their effects were represented using correction coefficients—γ and λ. Figure 15 presents a comparative analysis between the calculated and experimental results. The calculated values of the proposed bond strength

and bond slip equations for HSCFST aligned well with the experimental results (R^2 = 0.948). The average root mean square errors for the bond strength and bond slip equations were determined as 7.33% and 10.33%, respectively, indicating that the proposed equations can capture the overall variation trends of the interfacial bond parameters.

$$\tau_u = k\frac{1}{\gamma}\left[0.003T + 0.022f_{cu} + 0.0007\left(\frac{D}{t}\right)^2 - 0.082\left(\frac{D}{t}\right) + 1.152\right], \quad (10)$$

$$S_u = k\frac{1}{\lambda}\left[-0.079T - 0.237f_{cu} - 0.015\left(\frac{D}{t}\right) + 25.525\right], \quad (11)$$

where τ_u is the ultimate bond strength at the steel tube–concrete interface, S_u is the bond–slip value corresponding to the ultimate bond strength at the steel tube–concrete interface, γ is the correction factor used for τ_u calculation (1.055), λ is the correction factor used for S_u calculation (0.997), k is the influence coefficient of the steel tube surface condition (According to Xu et al. [37], k = 1.3 for a rusty steel tube surface, k = 1.0 for a rough steel tube surface after manual descaling, and k = 0.7 for a clean steel tube surface after mechanical descaling; the value of k is taken as 1.0 in this paper), D is the external steel tube diameter, t is the steel tube wall thickness, f_{cu} is the cubic compressive strength of the high-strength concrete, and T is the ambient temperature ($-60\ ^\circ\text{C} \leq T \leq 60\ ^\circ\text{C}$).

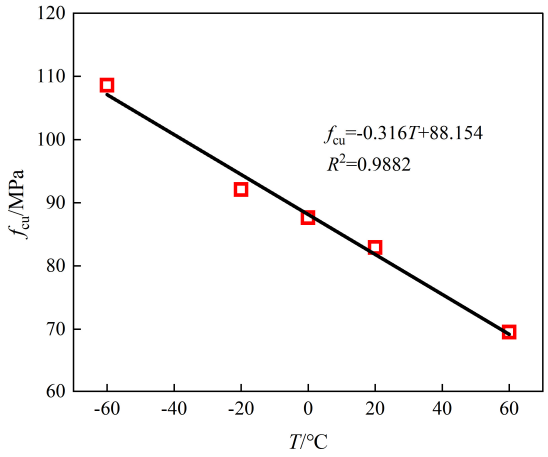


Figure 14. Influence of different ambient temperatures on the strength of concrete.

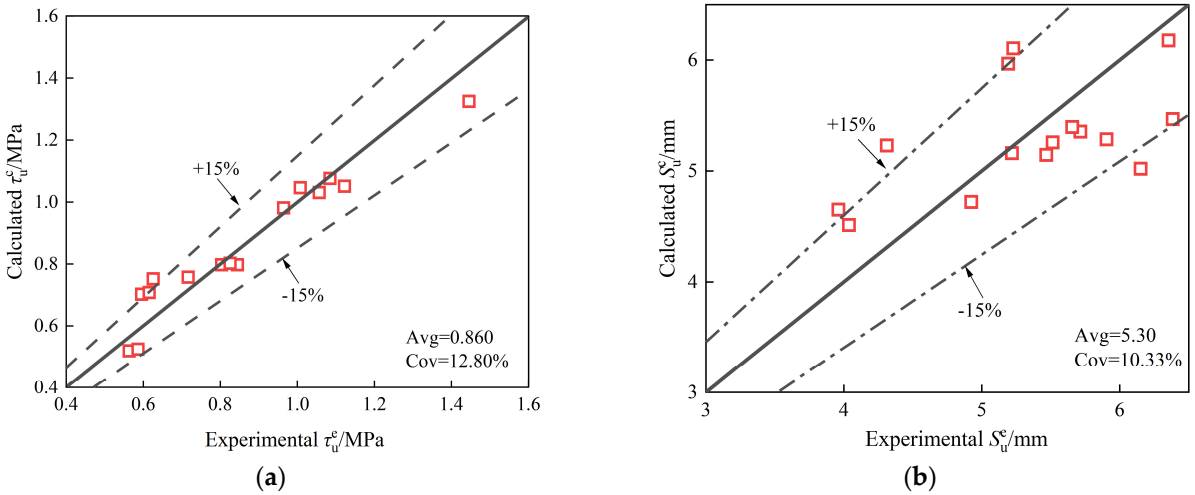


Figure 15. Comparison between calculated and experimental values of interfacial bond parameters: (**a**) ultimate bond strength, τ_u; (**b**) slip corresponding to the ultimate bond strength, S_u.

Considering that the regression equations were developed based on a limited number of experimental specimens, the statistical degrees of freedom were examined to evaluate the reliability of the regression analysis. For Equation (10), four independent variables, including ambient temperature (T), concrete compressive strength (f_{cu}), diameter-to-thickness ratio (D/t), and its quadratic term, were introduced. Therefore, the residual degrees of freedom were calculated as n − p − 1 = 15 − 4 − 1 = 10. For Equation (11), three independent variables were considered, resulting in a residual degree of freedom of 15 − 3 − 1 = 11. The obtained degrees of freedom indicate that the regression models retained sufficient statistical information for parameter estimation.

4.2.2. Leave-One-Out Cross-Validation Analysis

To further evaluate the generalization capability of the proposed regression equations, a leave-one-out cross-validation (LOOCV) analysis was performed. In each iteration, one specimen was selected as the validation sample, while the remaining specimens were used to establish the regression relationship. The obtained equation was subsequently used to predict the excluded specimen. This procedure was repeated until all specimens were independently evaluated.

The performance of LOOCV predictions was quantitatively evaluated using the coefficient of determination (R^2), root mean square error ($RMSE$), and mean absolute error (MAE), which were calculated as follows:

$$R^2 = 1 - \frac{\sum_{i=1}^{n} (y_i - \hat{y}_i)^2}{\sum_{i=1}^{n} (y_i - \overline{y})^2}, \tag{12}$$

$$RMSE = \sqrt{\frac{1}{n}\sum_{i=1}^{n} (y_i - \hat{y}_i)^2}, \tag{13}$$

$$MAE = \frac{1}{n}\sum_{i=1}^{n} |y_i - \hat{y}_i|, \tag{14}$$

where y_i and $\hat{y}_i$ represent the experimental and LOOCV-predicted values, respectively, $\overline{y}$ is the mean experimental value, and n is the number of specimens.

The quantitative evaluation results of the LOOCV predictions are summarized in Table 7, and the corresponding prediction results are presented in Figure 16. The calculated ultimate bond strength obtained from Equation (10) generally agrees well with the experimental values, and most specimens exhibit relatively small deviations. The quantitative evaluation results further indicate the stability of Equation (10) in predicting the ultimate bond strength under different temperature conditions.

Table 7. Quantitative evaluation results of the LOOCV analysis for the proposed equations.

Equation	Parameter	R^2	RMSE	MAE
Equation (10)	τ_u	0.8761	0.0865	0.0759
Equation (11)	S_u	−0.5037	0.9915	0.6770

Compared with Equation (10), the LOOCV results of Equation (11) show relatively larger deviations, indicating that the characteristic slip S_u exhibits higher dispersion than the ultimate bond strength. This difference may be attributed to the fact that S_u represents the deformation stage corresponding to ultimate bond strength, which is affected not only by temperature and geometric parameters but also by local interface conditions, concrete cracking development, and interfacial damage evolution.

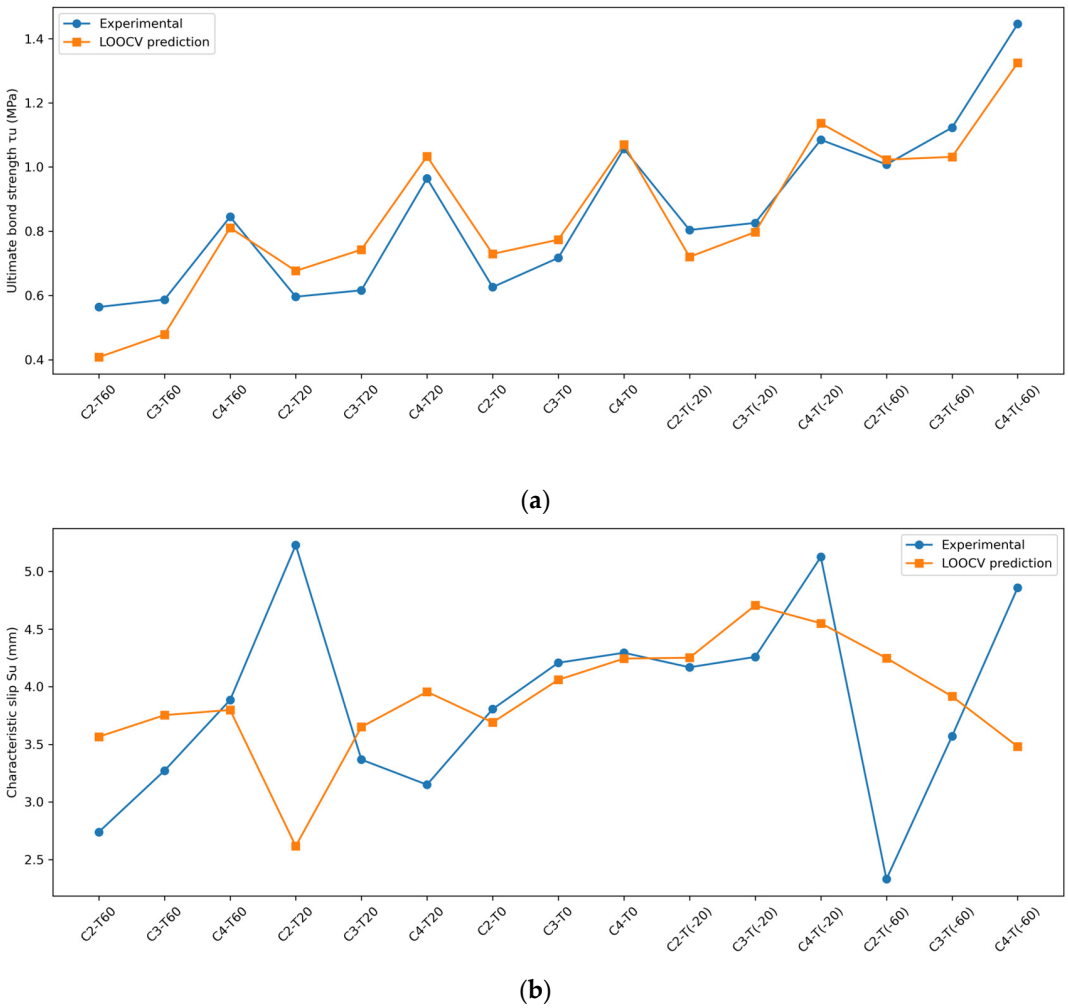


Figure 16. Leave-one-out cross-validation results for the proposed interfacial bond parameter equations: (**a**) ultimate bond strength, τ_u; (**b**) characteristic slip corresponding to the ultimate bond strength, S_u.

Therefore, Equation (10) can be considered as a relatively stable empirical relationship for estimating the ultimate bond strength, whereas Equation (11) should be regarded as an approximate relationship for characterizing the overall variation trend of characteristic slip rather than an accurate prediction model.

4.3. Bond Stress–Slip Constitutive Relationship

A combination of experimental methods, theoretical analysis, and numerical simulations is generally employed to study the interfacial bond–slip properties of CFST. The necessary conditions for an in-depth discussion on the interfacial bond–slip performance of CFST can be obtained by establishing an interfacial bond–slip constitutive relationship. Based on the experimental failure modes, the τ-S slip curves were categorized into three types, each representing three main stages of stress development—OA, AB (AC), and BC. Point A corresponds to the bond damage point, where the bond strength is τu and the slip is S_u. In type I, point B signifies the point where the curve begins to level off, with a bond strength of τum and a slip of Sum. In type II, point B represents the peak of the curve, where the bond strength is τ'_{um} and the slip is S'_{um}. Point C indicates the residual bond strength (τ_r) and corresponding slip amount (S_r) of the curve. According to existing studies [20,21,33,38,39] and Figure 7 of this paper, the τ-S curve of HSCFST was simplified (Figure 17).

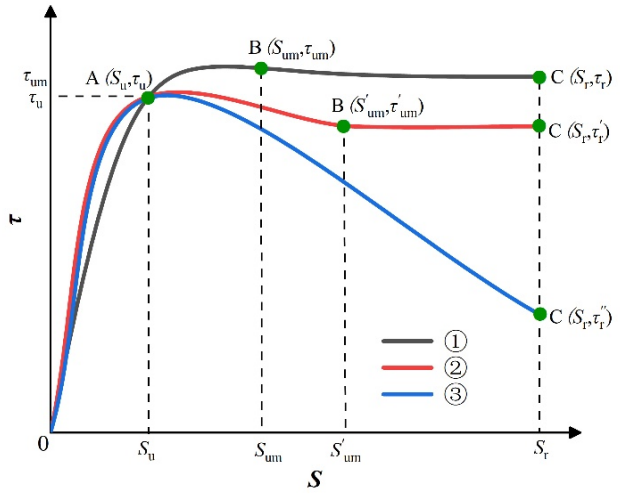


Figure 17. τ-S curve and characteristic points (Class I curve has no obvious peak value; there are obvious peaks in Classes II and III).

The bond transfer between the steel tube and concrete is primarily governed by chemical adhesion, mechanical interlocking, and friction. Under subzero temperatures, freezing of pore water at the interface may provide an additional contribution to the interfacial resistance. In low-temperature environments, the interfacial bond strength increases primarily due to the gradual transformation of water into ice below 0 °C, filling the voids within and on the surface of concrete. Steel tubes provide a relatively confined environment for the core concrete. At low temperatures, excess water freezes into ice adsorbed on the inner steel tube surface and fills the voids on the concrete surface, increasing the mechanical interlocking force at the steel tube–concrete interface. When the bond stress–slip curve of a concrete specimen reaches the ultimate bond strength, it exhibits three different trends. When the initial bond strength is less than the maximum static frictional force, the bond stress–slip curve is categorized as Type I, and when the combined effect of chemical adhesion and mechanical interlocking exceeds the maximum static frictional force, the bond stress–slip curve can be categorized as Type II or Type III.

(1) OA segment: The applied load continuously increased from point O to point A, whereas the initial stiffness changed little, indicating that no slip occurred at the steel tube–concrete interface. In this stage, chemical adhesion and frozen bond strength (at low temperatures) both played important roles. As the load continued to increase, slip occurred in local areas at both ends of the HSCFST column due to the failure of chemical adhesion, and mechanical interlocking force started to play a role. With a further increment in the applied load, the slip at both ends continued to increase and propagated to the middle region, where no slip occurred. When the slip reached point B, the anti-slip strength reached the maximum load, and simultaneously, chemical adhesion and mechanical interlocking jointly contributed to the interfacial resistance, while freezing of pore water may have provided an additional contribution under subzero temperatures.

(2) A-B-C segment: The entire steel tube–concrete interface experienced a slip after reaching the peak point, and the effect of chemical adhesion dissipated. Under conditions where the increase in load was insignificant, the increment of slip at the interface became quite large. In this stage, the mechanical interlocking force at the interface decreased significantly, and the interfacial bond strength was primarily supported by the frictional force at the interface. When the combined contributions of chemical adhesion and mechanical interlocking, together with the possible additional resistance associated with pore-water freezing under subzero temperatures, became

approximately comparable to the initial frictional resistance at the interface, the curve after the turning point became nearly a straight line (Type I in Figure 17). After point B, the stiffness of the Type II curve changed from positive to negative. During the anti-slip process, static friction disappeared and changed to kinetic friction to provide resistance. Sliding friction played an important role in the BC stage. After point C, chemical adhesion and mechanical engagement had largely degraded, leaving kinetic friction as the primary source of interfacial resistance, and the slope of the curve approached zero.

(3) AC segment: The entire steel tube–concrete interface experienced a slip after reaching the ultimate bond failure, and the slip at the interface continued to increase. Static friction changed to kinetic friction to provide resistance. The manufacturing tolerances of the steel pipe diameter and thickness along the height yielded sliding friction resistance, resulting in a distinct peak point on the curve followed by a descending segment (Type III in Figure 17).

$$\tau = \begin{cases} \left(\frac{S}{S_u}\right)^{\beta}\tau_u, & 0 < S < S_u, \quad \text{Segment OA} \\ \frac{S}{aS+b}, & S_u \le S \le S'_{um}, \quad \text{Segment AB, Type I} \\ cS + d, & S_u \le S \le S'_{um}, \quad \text{Segment AB, Type II} \\ \tau_r, & S_{um} \le S \le S_r, \quad \text{Segment BC, Type I/II} \\ c'S + d', & S'_{um} \le S \le S'_r, \quad \text{Segment AC, Type III} \end{cases}, \tag{15}$$

where $a = \frac{\frac{S_u}{\tau_u} - \frac{S_{um}}{\tau_{um}}}{S_u - S_{um}}$, $b = \frac{\left(\frac{S_u}{\tau_u}\right)S_{um} - \left(\frac{S_{um}}{\tau_{um}}\right)S_u}{S_{um} - S_u}$, $c = \frac{\tau'_r - \tau'_{um}}{S_r - S'_{um}}$, and $d = \frac{S_r\tau'_{um} - S'_{um}\tau_r}{S_r - S'_{um}}$. The values of τ_u and S_u were obtained from Equations (10) and (11), respectively. The values of τ_r, τ'_r, and τ''_r ($\tau_r = \tau_{um}$ and $\tau'_r - \tau'_{um}$) were determined by tests, and the value of S_r was 30 mm. The coefficients of the computational model for each stage were obtained through regression fitting.

$$a = -0.007S_u + 0.137\tau_u - 0.004S_{um} - 1.037\tau_{um} + 2.007, \tag{16}$$

$$b = 0.25S_u - 4.812\tau_u - 0.018S_{um} + 3.425\tau_{um} + 0.891, \tag{17}$$

$$c = 0.001S_u - 0.044\tau_u + 0.039\tau'_{um} - 0.008, \tag{18}$$

$$d = 0.001S_u + 1.21\tau_u - 0.001S_u - 0.169\tau'_{um} - 0.001, \tag{19}$$

$$c' = -0.041\tau_u + 0.041\tau''_r + 0.001, \tag{20}$$

$$d' = 0.007S_u + 1.239\tau_u - 0.234\tau''_r - 0.043, \tag{21}$$

As shown in Table 8, the fitted values of β ranged from 0.890 to 1.528, while the corresponding R^2 values ranged from 0.857 to 0.970. The arithmetic mean of the fitted β values was 1.172. Figure 18a,b shows that no systematic dependence of β on either D/t or ambient temperature T could be identified from the present dataset. In the original constitutive formulation, β = 1.172 was adopted as a representative value to simplify the implementation of the bond–slip model.

According to the ascending branch of the proposed bond stress–slip constitutive model, the normalized relationship can be expressed as

$$\frac{\tau}{\tau_u} = \left(\frac{S}{S_u}\right)^{\beta}, \tag{22}$$

To quantify the influence of the observed variability in β, a constitutive-level sensitivity analysis was performed using β = 0.890, 1.172, and 1.528, corresponding to the minimum,

arithmetic mean, and maximum values obtained from the tested specimens, respectively. As shown in Figure 19, β mainly affects the shape of the early and intermediate portions of the ascending branch. At S/S_u = 0.50, the normalized bond stress τ/τ_u is 0.540, 0.444, and 0.347 for β = 0.890, 1.172, and 1.528, respectively. At S/S_u = 0.90, the corresponding values are 0.910, 0.884, and 0.851. The influence of β therefore decreases as the slip approaches S_u, and all curves converge to τ/τ_u = 1.0 at S/S_u = 1.0. These results indicate that β primarily controls the pre-peak shape and local interfacial stiffness of the ascending branch, whereas it does not change the prescribed peak bond strength τu or the corresponding characteristic slip S_u. Accordingly, the arithmetic mean value β = 1.172 was adopted as the representative parameter in the simplified constitutive model.

Table 8. Results of β values for all specimens.

Label	β	R^2
C2-T60	1.089	0.968
C3-T60	1.127	0.966
C4-T60	1.088	0.964
C2-T20	0.902	0.933
C3-T20	1.105	0.953
C4-T20	1.420	0.964
C2-T0	1.026	0.950
C3-T0	0.890	0.938
C4-T0	1.200	0.961
C2-T(−20)	1.165	0.951
C3-T(−20)	1.229	0.945
C4-T(−20)	1.136	0.857
C2-T(−60)	1.373	0.970
C3-T(−60)	1.528	0.955
C4-T(−60)	1.306	0.948

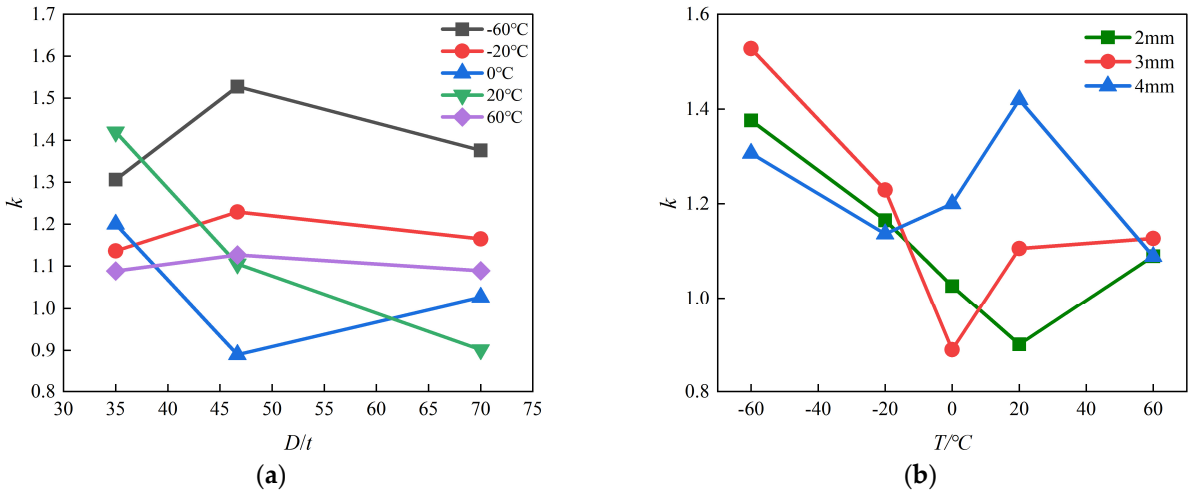


Figure 18. Effects of diameter-to-thickness ratio (D/t) and ambient temperature on the β value: (**a**) effect of D/t; (**b**) effect of ambient temperature.

Because the force–displacement relationship assigned to each nonlinear connector spring was directly derived from the bond stress–slip constitutive relationship, the normalized sensitivity to β is inherited by the local connector response. In other words, variation in β changes the pre-peak force–displacement shape of an individual connector but does not change its prescribed characteristic peak force or the corresponding characteristic displacement. The present sensitivity analysis therefore quantifies the influence of β on

the local connector constitutive response. It should be noted, however, that it does not constitute a new sensitivity analysis of the global finite element load–slip response.

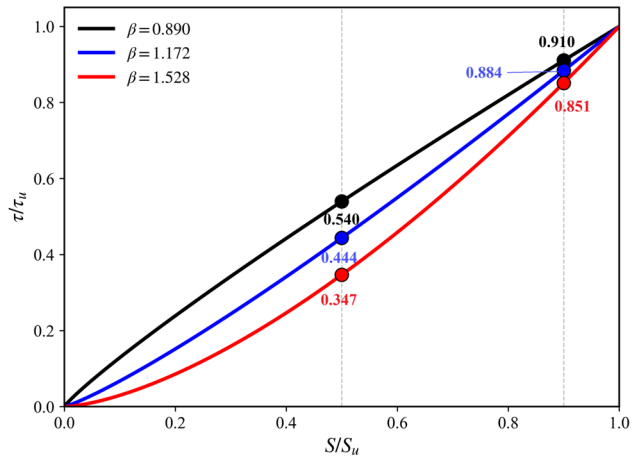


Figure 19. Sensitivity analysis of the normalized ascending branch of the bond stress–slip relationship to parameter β.

According to the bond stress–slip constitutive relationship model of the specimens, the fitting curves for the basic group of specimens were plotted and compared with the experimental curves for verification (Figure 20). The constitutive model curves matched well with the overall trend of the experimental curves, indicating that the bond stress–slip constitutive model for HSCFST proposed in this paper can effectively describe the entire process of interface bond slip failure under different ambient temperatures. Hence, this model can be used as a reference in practical engineering applications and finite element simulations.

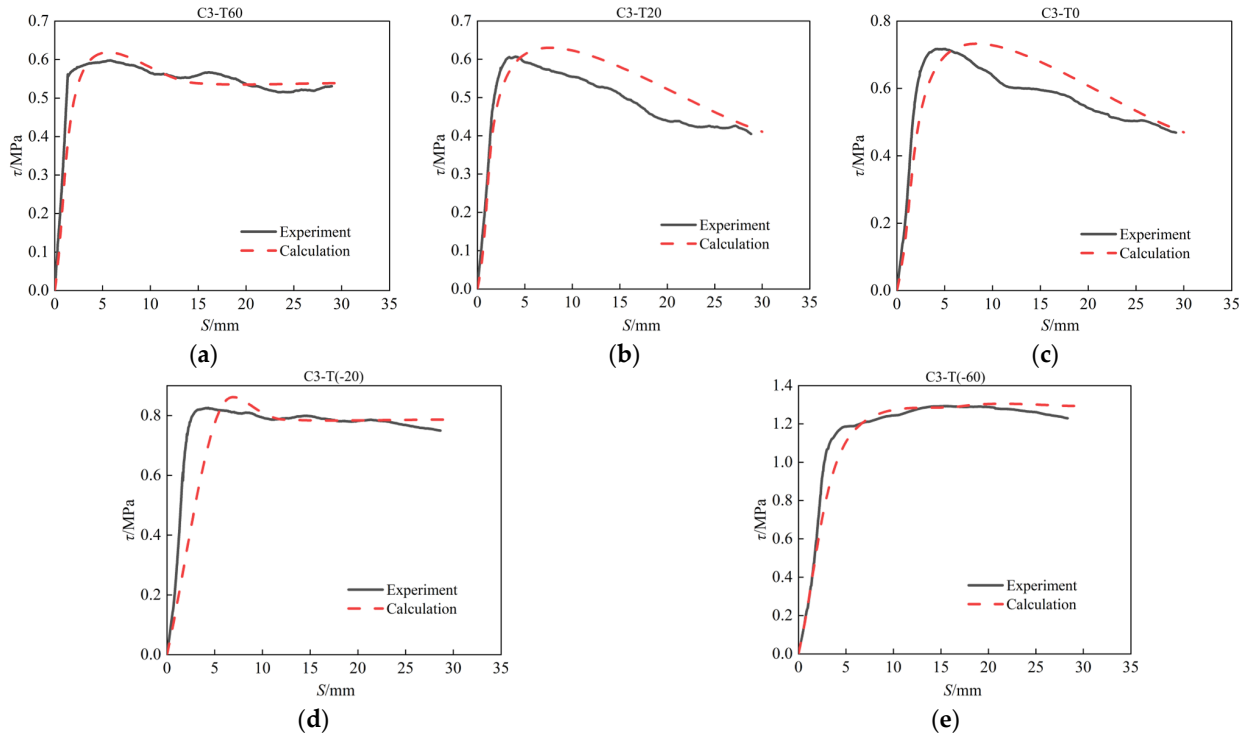


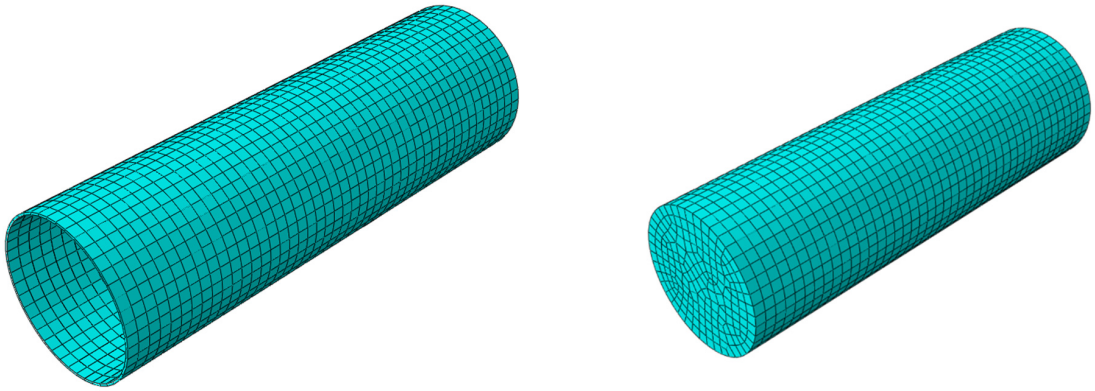
Figure 20. Comparison between calculated constitutive curves and experimental curves of C3 specimens under different ambient temperatures: (**a**) C3-T60; (**b**) C3-T20; (**c**) C3-T0; (**d**) C3-T(−20); (**e**) C3-T(−60).

5. Finite Element Analysis

5.1. Finite Element Modeling

5.1.1. Element Type and Mesh Size

Numerical models for push-out tests of HSCFST specimens with different interfaces were developed using ABAQUS/Standard 2024. The steel tube was modeled using 4-node reduced integration shell elements (S4R). In order to enhance computational accuracy, a 9-point Simpson integration scheme was applied in the thickness direction of the shell elements. The core concrete was modeled using 8-node reduced integration three-dimensional solid elements (C3D8R). Figure 21 illustrates the specific mesh division of the numerical model.



(**a**) (**b**)

Figure 21. Finite element mesh of the HSCFST specimen: (**a**) steel tube; (**b**) core concrete.

A mesh convergence study was conducted using characteristic mesh sizes of 5, 10, 20, and 30 mm. The 5 mm mesh was taken as the reference solution, and the relative deviations in the characteristic load Pu and the corresponding slip Su were used to evaluate mesh convergence. A relative deviation of 5% was adopted as the quantitative acceptance criterion. As summarized in Table 9, the 10 mm mesh produced deviations of only 1.39% in Pu and 0% in Su relative to the 5 mm reference mesh, satisfying the adopted convergence criterion for both quantities. Although the coarser 20 and 30 mm meshes showed similarly small deviations in Pu, their deviations in Su exceeded 5%. The influence of mesh size on the load–slip response is illustrated in Figure 22.Therefore, considering both numerical accuracy and computational efficiency, a mesh size of 10 mm × 10 mm × 10 mm was adopted for the subsequent finite element analyses.

$$\delta_X = \frac{|X_h - X_{\text{ref}}|}{X_{\text{ref}}} \times 100\%, \tag{23}$$

where X_h is the result obtained using the investigated mesh size and X_{ref} is the result obtained using the 5 mm reference mesh.

Table 9. Mesh convergence study of the finite element model.

Mesh Size (mm)	P_u (kN)	Deviation in P_u (%)	S_u (mm)	Deviation in S_u (%)
5	143.7982	—	5.5	—
10	145.7983	1.39	5.5	0.00
20	145.7983	1.39	6.0	9.09
30	145.7983	1.39	6.2	12.73

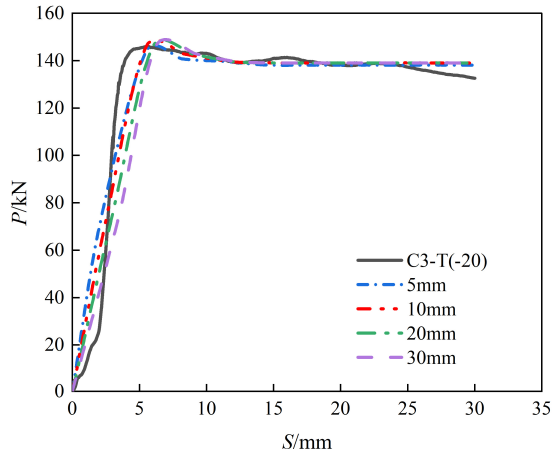


Figure 22. Effect of mesh size.

The steel tube was modeled using its nominal ideal geometry, and no initial geometric imperfection was explicitly introduced. Accordingly, neither an eigenmode-based imperfection shape nor a prescribed imperfection amplitude was assigned in the present finite element model. This simplification was considered acceptable for the present push-out analysis because no evident local buckling of the steel tubes was observed in the tests and the numerical investigation focused primarily on interfacial bond transfer rather than steel-tube instability.

5.1.2. Temperature-Dependent Constitutive Models

(1) Constitutive model of steel

The constitutive model of steel under the effect of ambient temperature consisted of five stages—elastic stage (oa), elastic–plastic stage (ab), plastic stage (bc), hardening stage (cd), and second flow plasticity stage (de) [40] (Figure 23). The mathematical expression for the constitutive model of steel is presented in Equation (19), where the variables were derived from experimental measurements. The resulting stress–strain relationship curve for steel under the effect of ambient temperature is displayed in Figure 23.

$$\sigma_s^T = \begin{cases} E_s^T \varepsilon_s^T, & \left(\varepsilon_s^T < \varepsilon_e^T\right) \\ -A\left(\varepsilon_s^T\right)^2 + B\left(\varepsilon_s^T\right) + C, & \left(\varepsilon_e^T \le \varepsilon_s^T < \varepsilon_{e1}^T\right) \\ f_y^T, & \left(\varepsilon_{e1}^T \le \varepsilon_s^T < \varepsilon_{e2}^T\right), \\ f_y^T\left(1 + 0.6\frac{\varepsilon_s^T - \varepsilon_{e2}^T}{\varepsilon_{e3}^T - \varepsilon_{e2}^T}\right), & \left(\varepsilon_{e2}^T \le \varepsilon_s^T < \varepsilon_{e3}^T\right) \\ 1.6 f_y^T, & \left(\varepsilon_s^T \ge \varepsilon_{e3}^T\right) \end{cases} \tag{24}$$

where $\varepsilon_e^T = \frac{0.8 f_y^T}{E_s^T}$, $\varepsilon_{e2}^T = 10\varepsilon_{e1}^T$, $\varepsilon_{e3}^T = 100\varepsilon_{e1}^T$, $A = \frac{0.2 f_y^T}{\varepsilon_{e1}^T - \varepsilon_e^T}$, $B = 2A\varepsilon_{e1}^T$, $C = 0.8 f_y^T + A\left(\varepsilon_e^T\right)^2 + B\varepsilon_e^T$, σ_s^T, E_s^T, and f_y^T are the stress strength (MPa), elastic modulus (GPa), and yield strength (MPa) of steel, respectively, and T is the test temperature (°C).

(2) Constitutive model of concrete

Considering the significant impact of temperature on concrete strength and the restraining effect of steel tubes on concrete, the plastic damage model within ABAQUS software [41,42] was adopted to construct the constitutive model of concrete. The model parameters were defined as follows: a dilation angle of 35°, an eccentricity of 0.1, a ratio of biaxial to uniaxial compressive strength (f_{b0}/f_{c0}) of 1.1667, and a viscosity parameter of 0.005. The intrinsic model of steel tube-restrained concrete proposed by Han [40] can be

used to simulate the restraining effect of steel tubes on concrete and also to represent the residual stage of short columns. Hence, based on the stress–strain relationship for CFST proposed by Han [40], a uniaxial compressive stress–strain (σ-ε) constitutive model under the influence of ambient temperature was derived (Figure 24). The mechanical properties of the core concrete varied with ambient temperature. At the elevated temperature of 60 °C, the reduction in elastic modulus resulted from the evaporation of capillary pore water, which increased the pore pressure and weakened the bonding force. In contrast, under subzero-temperature conditions, the free water within concrete pores froze (the ice volume expanded by approximately 9%) and generated internal frost heave stress, which consequently increased the elastic modulus of the core concrete.

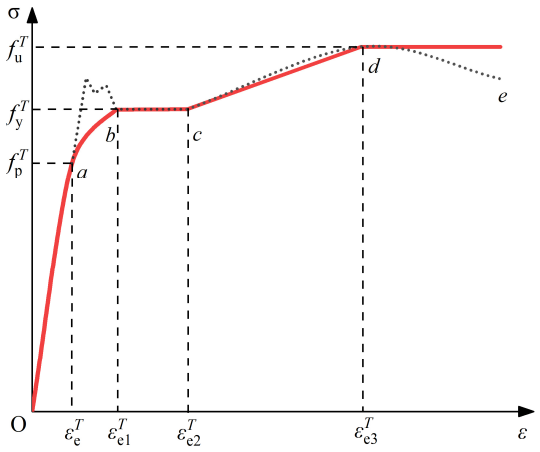


Figure 23. Constitutive model of steel under different temperatures. The red solid line represents the idealized constitutive model adopted in the finite element analysis, while the dotted line indicates the corresponding experimental stress-strain response.

$$y^T = \begin{cases} 2x^T - (x^T)^2, & (x^T \le 1) \\ \dfrac{x^T}{\beta^T (x^T - 1)^\eta + x^T}, & (x^T > 1), \end{cases} \tag{25}$$

where $x^T = \frac{\varepsilon}{\varepsilon_0^T}$ and $y^T = \frac{\sigma}{\sigma_0^T}$.

$$\sigma_0^T = f_c^T (1.15 - 0.0052T), \tag{26}$$

$$\begin{cases} \varepsilon_c = (1300 + 12.5 f_c^T) \\ \varepsilon_0^T = (\varepsilon_c + 800\xi^{0.2})(9.26 \times 10^{-5} T^2 + 0.015T + 0.69) \times 10^{-6} \end{cases}, \tag{27}$$

$$\beta^T = \left(2.36 \times 10^{-5}\right)^{[0.25 + (\xi - 0.5)^7]} \cdot \left(f_c^T\right)^{0.5} \cdot 0.5, \tag{28}$$

where β^T reflects the ductility of the core concrete and the amount of absorbed energy, ξ is the hoop coefficient of the specimen and $\eta = 2$.

$$\xi^T = \frac{A_s f_y^T}{A_c f_c^T} = \alpha \frac{k_y(T) f_y^{20}}{k_c(T) f_c^{20}}, \tag{29}$$

where A_s is the cross-section area of the steel tube (mm^2), A_c is the cross-section area of the core concrete (mm^2), α represents the steel content in the cross section of the HSCFST specimen.

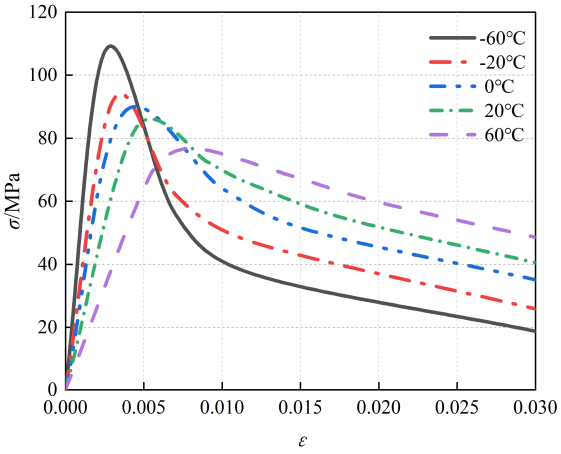


Figure 24. Stress-strain curve of core concrete considering temperature.

Based on the experimental data obtained in this study, temperature reduction coefficients for the yield strength of structural steel and the axial compressive strength of concrete were derived through curve fitting.

$$k_y(T) = 1 - 0.001504(T - 20) + 1.832 \times 10^{-5}(T - 20)^2, \tag{30}$$

$$k_c(T) = 1 - 0.00479(T - 20) + 7.42 \times 10^{-6}(T - 20)^2, \tag{31}$$

Yield strength of steel at various temperatures and axial compressive strength of concrete.

$$f_y^T = f_y^{20} k_y(T), \tag{32}$$

$$f_c^T = f_c^{20} k_c(T), \tag{33}$$

where, f_y^{20} and f_c^{20} are, respectively, 20 °C (normal temperature) steel yield strength and core concrete axial compressive strength (MPa). The concrete compressive strength obtained from the cube compression tests was taken as the cube compressive strength at 20 °C, f_{cu}^{20}. Since the temperature-dependent constitutive model requires the axial compressive strength, the measured cube compressive strength was converted into the axial compressive strength f_c^{20} according to the relationship specified in the Chinese code GB 50010-2010 [43]:

$$f_c^{20} = 0.88\alpha_{c1}\alpha_{c2} f_{cu}^{20}$$

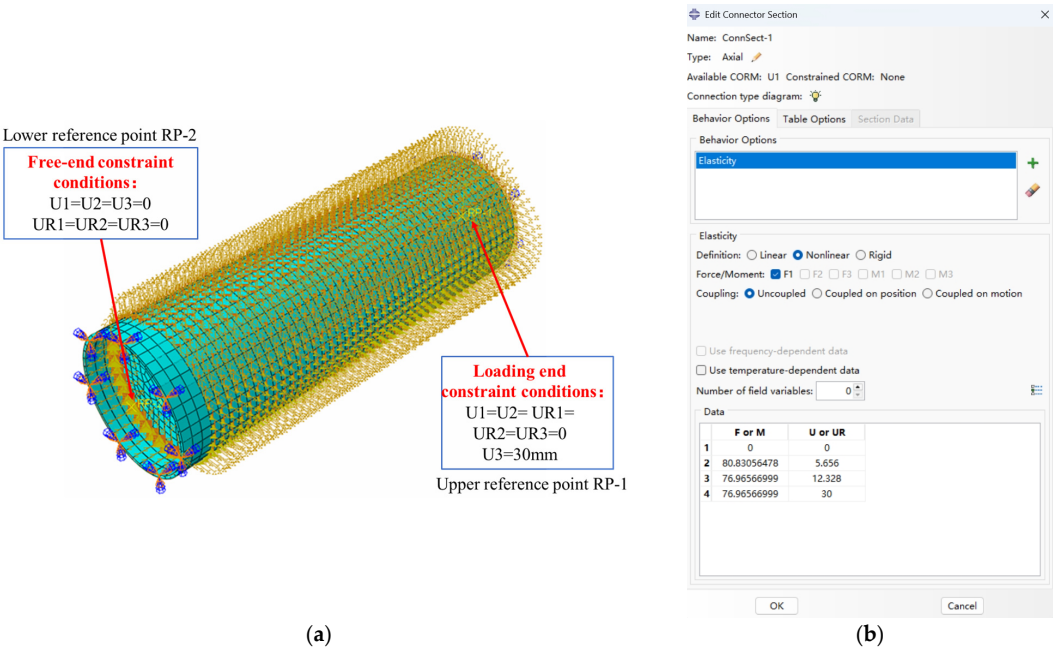
where f_c^{20} represents the axial compressive strength of concrete at 20 °C, f_{cu}^{20} denotes the cube compressive strength at 20 °C, and α_{c1} and α_{c2} are the corresponding conversion coefficients. According to the Commentary to Clause 4.1.3 of GB 50010-2010, α_{c1} is taken as 0.76 for concrete strength grades up to C50 and 0.82 for C80, with linear interpolation for strength grades between C50 and C80; α_{c2} is taken as 1.00 for C40 and 0.87 for C80, with linear interpolation for strength grades between C40 and C80. The converted axial compressive strengths were subsequently adopted in the temperature-dependent constitutive model, and the corresponding values are summarized in Table 5.

5.1.3. Interaction and Boundary Conditions

Due to the nonlinearity of materials and the influence of temperature on HSCFST, the interfacial force transmission becomes highly complex, and a simple linear relationship cannot accurately represent the actual behavior of the steel tube–concrete interface. Therefore, nonlinear spring connectors were employed to simulate the bond stress–slip behavior at the steel tube–concrete interface. In ABAQUS, a conventional approach in-

volves initially introducing linear spring elements and subsequently modifying the .inp file to define nonlinear behavior. Although this method is relatively straightforward, it may lead to convergence difficulties during analysis. To overcome this issue, nonlinear spring connectors were directly established between the coincident nodes of the steel tube and the core concrete to simulate the interfacial bonding behavior.

Contact spring connectors were defined at the steel tube–concrete interface in both longitudinal and tangential directions. A Python script (Python 3.10) was developed to automatically generate the connector elements, resulting in a total of 1806 nonlinear springs for the reference specimen group. These connectors were evenly and symmetrically distributed within the bonded region, with their orientations aligned with the loading direction of the concrete. The bond behavior was characterized by assigning the force–displacement relationship obtained from the bond stress–slip constitutive model (Section 4.3) to the connector elements (Figure 25). The force–displacement relationship of each individual connector was determined by dividing the total bond force derived from the constitutive model by the total number of connectors. Since the normal slip was significantly smaller than the tangential slip, hard contact was adopted to describe the normal interaction between the steel tube and concrete. In addition, a steel plate was placed beneath the steel tube, and an anchor with a slightly smaller diameter than the steel tube diameter was positioned above the concrete. A vertical displacement load was applied at the loading end anchor in the Z direction, resulting in deformation only along the U3 direction (U3 = 30 mm; U1 = U2 = UR1 = UR2 = UR3 = 0). The free end of the specimen was fully constrained (U1 = U2 = U3 = UR1 = UR2 = UR3 = 0). A shell-to-solid coupling constraint was applied between the base plate and the steel tube. The loading end was coupled with reference point RP-1, while the base plate–steel tube assembly was coupled with reference point RP-2. The displacement load was applied through RP-1, and the fixed boundary condition was imposed at RP-2.



(**a**) (**b**)

Figure 25. Definition of interface interaction and boundary conditions for the HSCFST finite element model: (**a**) arrangement of connector spring elements at the steel tube–concrete interface and displacement boundary conditions at the reference points; (**b**) definition of bond–slip parameters for the connector section.

In the present finite element model, the steel–concrete interface behavior was represented using an equivalent homogenized connector formulation. Under the same interface

condition, identical force–displacement relationships were assigned to the connector elements, without explicitly considering the spatial variation in local bond properties along the bonded length. This simplification was adopted because the objective of the numerical model was to reproduce the global bond-transfer behavior, including the overall load–slip response and characteristic bond resistance, rather than to reconstruct the detailed local bond-stress distribution at every position along the interface. Considering that the push-out test provides a global bond stress–slip relationship, the equivalent average bond–slip law is considered appropriate for evaluating the overall interfacial response.

The finite element analysis did not explicitly simulate the thermal loading process or the thermal strains induced by differential thermal expansion between the steel tube and the core concrete. Instead, each target temperature was treated as an independent isothermal mechanical condition. The experimentally determined temperature-dependent material properties of steel and concrete, together with the temperature-dependent bond–slip constitutive relationship, were assigned to the corresponding finite element model. The subsequent push-out process was then simulated by applying the prescribed axial displacement. Therefore, the numerical model was intended to reproduce the mechanical response of HSCFST specimens after conditioning to a given temperature, rather than the transient thermo-mechanical response during heating or cooling.

5.2. Model Calibration and External Assessment

The finite element model was first assessed against the 15 specimens tested in the present study. Because the constitutive parameters and connector properties were derived from the same experimental dataset, this comparison is regarded as a calibration-based consistency assessment rather than an independent validation. The comparison was used to examine whether the numerical model could reproduce the experimentally observed load–slip response and characteristic loads.The comparisons between the FEA results and experimental load-slip curves for specimens under different temperatures are presented in Figure 26, and the corresponding quantitative comparisons are summarized in Table 10.

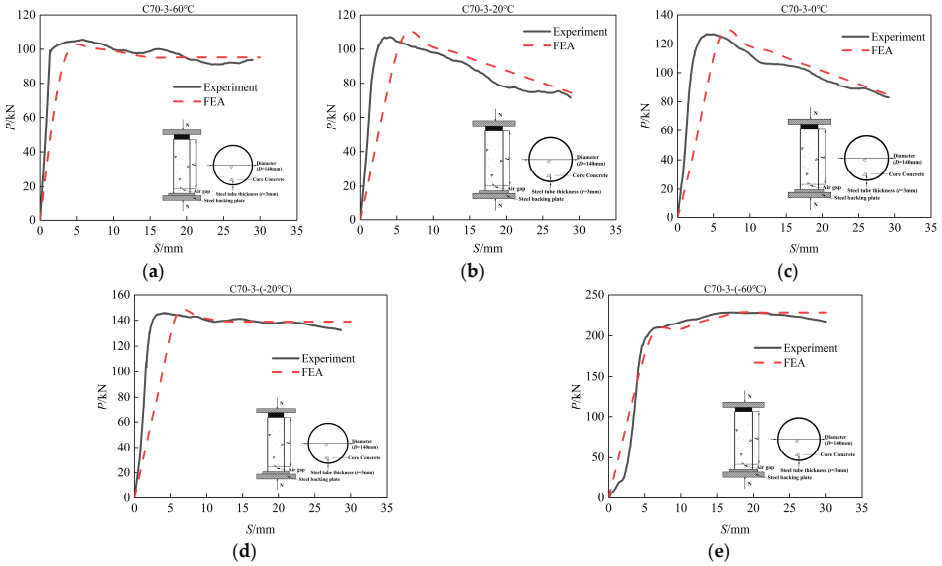


Figure 26. Comparison between finite element analysis (FEA) and experimental load–slip curves of HSCFST specimens under different ambient temperatures: (**a**) 60 °C; (**b**) 20 °C; (**c**) 0 °C; (**d**) −20 °C; (**e**) −60 °C.

To further assess the transferability of the modeling approach, additional comparisons were conducted using the experimental data reported by Yan et al., which were not included in the present model calibration. It should be noted, however, that these specimens extend

beyond the calibration domain of the present study. In particular, the Yan et al. dataset includes a specimen tested at −80 °C and specimens made with C45 concrete, whereas the present model was calibrated using HSCFST specimens within −60 °C to 60 °C and concrete strengths of approximately 69.5–108.6 MPa. Therefore, this comparison is regarded as an external extrapolative assessment rather than an independent validation within the calibrated parameter range.The comparison between the FEA predictions and the experimental load-slip curves reported by Yan et al. is shown in Figure 27.

Table 10. Comparison of experimental data with finite element analysis.

Reference	Label	$D \times t \times L_i$/mm	T/°C	P_u^e/kN	P_u^a/kN	P_u^e/P_u^a	Role in Model Assessment
This paper	C2-T60	140 × 2 × 420	60	101.26	100.09	1.01	Calibration assessment
	C3-T60	140 × 3 × 420	60	103.81	102.95	1.01	
	C4-T60	140 × 4 × 420	60	147.26	153.00	0.96	
	C2-T20	140 × 2 × 420	20	106.94	108.05	0.99	
	C3-T20	140 × 3 × 420	20	108.91	110.33	0.99	
	C4-T20	140 × 4 × 420	20	168.06	169.44	0.99	
	C2-T0	140 × 2 × 420	0	112.33	114.97	0.98	
	C3-T0	140 × 3 × 420	0	126.83	130.22	0.97	
	C4-T0	140 × 4 × 420	0	184.09	186.17	0.99	
	C2-T(−20)	140 × 2 × 420	−20	144.30	142.33	1.01	
	C3-T(−20)	140 × 3 × 420	−20	145.98	149.66	0.98	
	C4-T(−20)	140 × 4 × 420	−20	188.95	186.25	1.01	
	C2-T(−60)	140 × 2 × 420	−60	180.85	184.06	0.98	
	C3-T(−60)	140 × 3 × 420	−60	198.61	208.38	0.95	
	C4-T(−60)	140 × 4 × 420	−60	251.90	248.25	1.01	
Yan [20]	C1	133 × 4.5 × 360	−60	301.52	299.48	1.01	External extrapolative assessment
	C4	133 × 4.5 × 360	−80	335.18	330.18	1.02	
	C7	133 × 4.5 × 360	−60	308.81	309.22	1.00	
	C8	133 × 5.75 × 360	−60	371.02	369.23	1.00	
	C10	133 × 4.5 × 560	−60	497.39	488.42	1.02	

5.3. Stress Distribution and Failure Modes

The stress distributions shown in Figures 28–30 represent the mechanical stresses developed during the push-out process under temperature-dependent material and interface properties. Thermal stresses generated directly by differential thermal expansion or contraction were not explicitly included in the present finite element model. The interfacial stress of the HSCFST specimens exhibited a uniform, ring-shaped distribution (Figure 28); especially, the longitudinal stress in the steel tube steadily increased from the loading end to the free end. It should be noted that stress concentration occurred at the free end of the empty steel tube, and this phenomenon was reflected in the deformation patterns observed in the experimental results. In contrast, the longitudinal stress in the core concrete gradually decreased from the loading end to the free end, and local stress concentration was observed at the loading end, further corroborating the experimental findings. During the push-out process, the steel tube remained within the elastic range. Figure 30 presents the finite element results of some of the test data from the study of Yan [20] at low temperatures simulated with the constitutive relationship proposed in this paper. As the specimen was in an ultra-low-temperature environment and the concrete had a low-strength grade with high water content, large freezing bonds were created in the low-temperature environment, and local inhomogeneity and stress concentration occurred at the loaded and free ends of the steel tube and the core concrete.

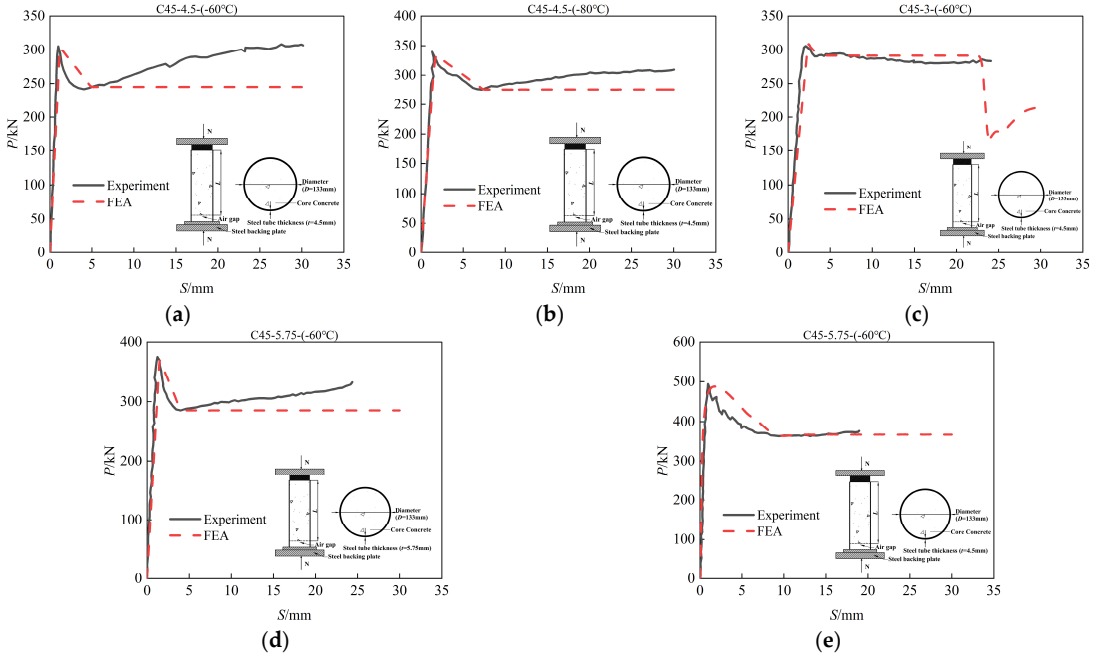


Figure 27. Comparison between finite element analysis (FEA) results and experimental load–slip curves reported by Yan et al.: (**a**) C1; (**b**) C4; (**c**) C7; (**d**) C8; (**e**) C10.

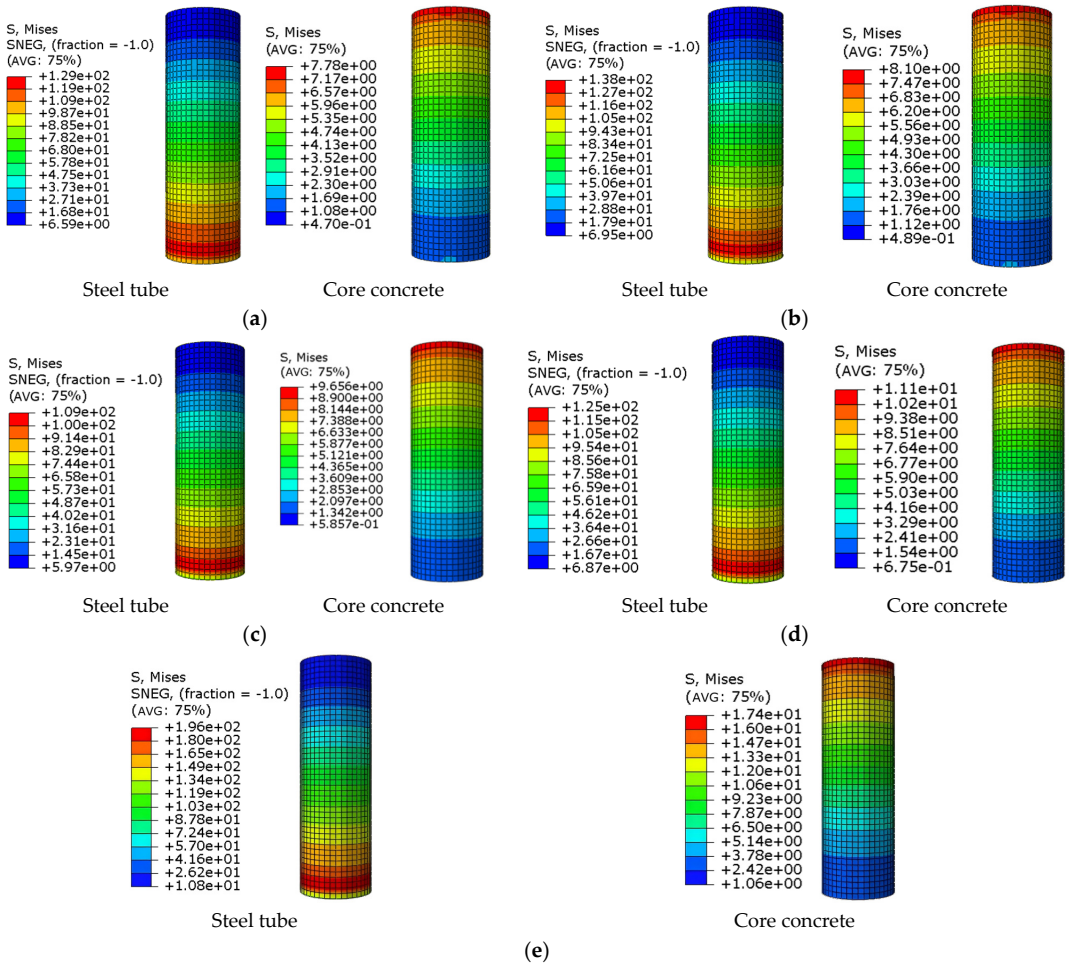


Figure 28. von Mises stress distributions of the steel tube and core concrete in HSCFST specimens under different ambient temperatures: (**a**) 60 °C; (**b**) 20 °C; (**c**) 0 °C; (**d**) −20 °C; (**e**) −60 °C. For each

temperature condition, the left and right contours represent the steel tube and core concrete, respectively.

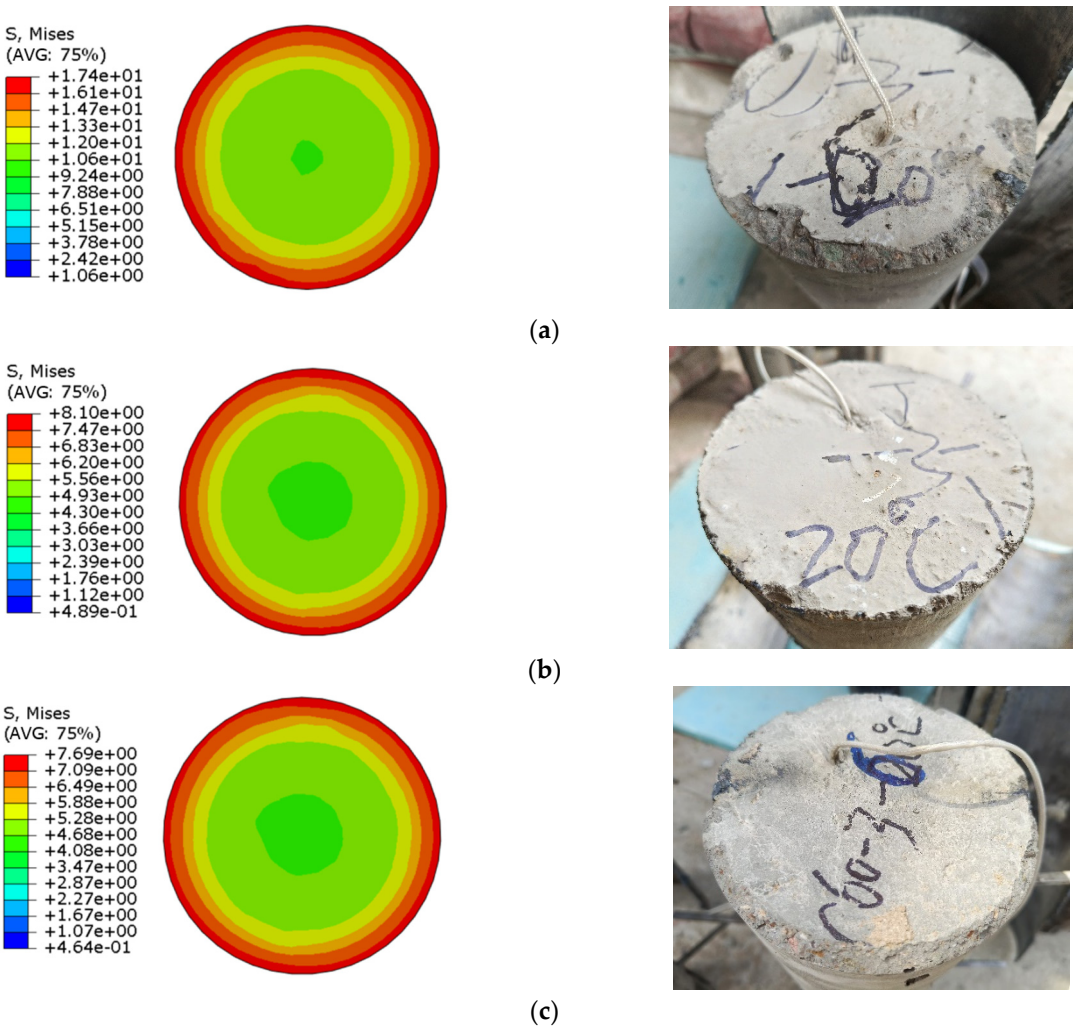


Figure 29. Comparison between finite element stress distributions and experimental failure morphology at the loaded end of core concrete under different ambient temperatures: (**a**) low-temperature condition, C3-T(−60); (**b**) normal-temperature condition, C3-T20; (**c**) high-temperature condition, C3-T60. For each condition, the left panel shows the finite element von Mises stress distribution, and the right panel shows the corresponding experimental failure morphology.

The present finite element analysis primarily focused on the global bond-transfer response and stress distributions in the steel tube and core concrete. A detailed quantitative interpretation of plastic-strain localization and concrete damage evolution was beyond the scope of the present model; therefore, PEEQ and damage-variable contours were not used to infer the local failure mechanism.

It should be emphasized that Figures 28–30 show the von Mises stress fields in the steel tube and core concrete rather than the spatial distribution of local connector bond stresses. Consequently, these figures are used to illustrate the overall load-transfer path and stress-concentration regions predicted by the equivalent-interface model. They should not be interpreted as a direct quantitative representation or validation of the actual nonuniform local bond-stress distribution along the steel-concrete interface.

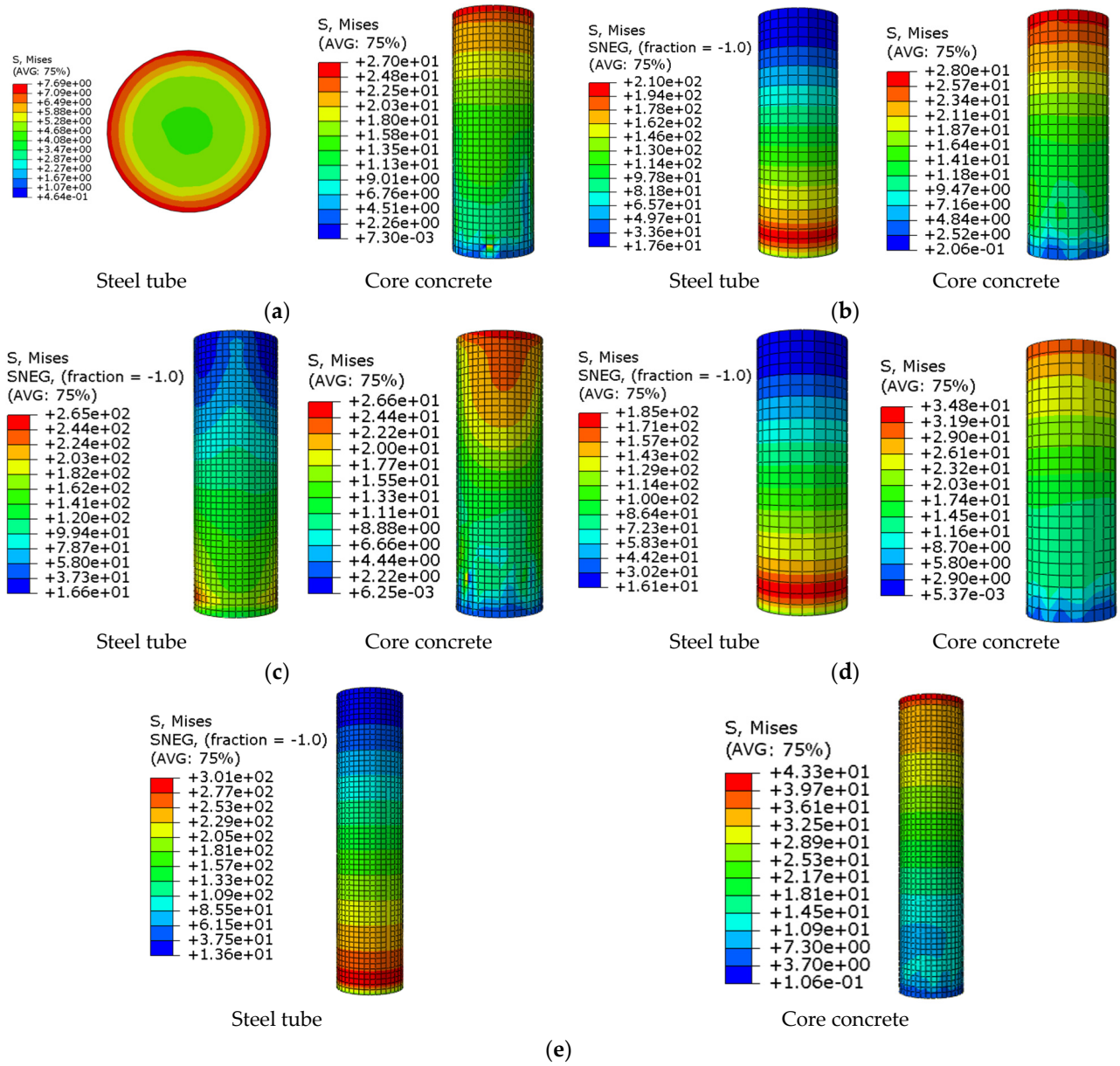


Figure 30. von Mises stress distributions of specimens from the experimental data reported by Yan et al.: (**a**) C1; (**b**) C4; (**c**) C7; (**d**) C8; (**e**) C10. For each specimen, the left and right contours represent the steel tube and core concrete, respectively.

6. Conclusions

The temperature-dependent interfacial bond behavior of HSCFST members was examined through push-out tests and finite element analysis. The main conclusions are as follows.

(1) Push-out tests on 15 HSCFST specimens revealed an inverse relationship between ambient temperature and interfacial bond strength. Compared with the value at 20 °C, the bond strength decreased by 4.71% at 60 °C but increased by 82.31% at −60 °C. Although low temperatures enhanced the bond resistance of HSCFST members, the increase was less pronounced than that reported for conventional CFST members, which may be attributed to the influence of the lower water–cement ratio of high-strength concrete on freezing-induced interfacial bonding.

(2) A multivariable regression framework was established to quantify the simultaneous effects of ambient temperature, concrete compressive strength, and the steel tube

diameter-to-thickness ratio on interfacial bond strength. With a root-mean-square error below 7.33%, the proposed formulation showed good consistency with both the present experimental results and existing prediction models.

(3) The measured interface response was characterized by three main stages of stress development—OA, AB (AC), and BC—based on the characteristic points of the bond stress–slip curves. A piecewise constitutive relationship was subsequently formulated to represent the complete bond–slip process.

(4) Bond transfer at the steel–concrete interface was represented in ABAQUS by distributed nonlinear connector elements. The numerical analysis reproduced the principal features of the measured load–slip response with a mean peak-load deviation of 1.66%, while discrepancies for the remaining characteristic loads remained below 5%. Additional comparison with the independent data reported by Yan et al. showed that the modeling approach could reasonably reproduce the overall response even under extrapolative conditions; however, these specimens partly fall outside the temperature and concrete-strength ranges used for model calibration, and the results should therefore be interpreted with caution.

Limitations and Future Work

Several limitations should be acknowledged in the present study. First, only one specimen was tested for each temperature and steel tube thickness condition, and the effects of temperature and concrete strength could not be completely separated in the experimental design. Further tests involving replicated specimens and different concrete grades under identical thermal conditions are needed to improve statistical reliability and clarify individual influencing mechanisms.

Second, the present tests mainly considered specimens under approximately uniform and stable temperature conditions, whereas practical HSCFST members may experience transient and nonuniform thermal fields. Future studies should consider temperature gradients and thermal cycling to further improve the engineering applicability of the proposed model. In addition, the proposed freezing-related interfacial mechanism was inferred from post-test observations and requires further verification through in situ monitoring techniques.

Third, several simplifications were introduced in the finite element model. The steel tube was modeled using nominal geometry without explicitly considering manufacturing-induced imperfections, and the local interface properties were homogenized along the bonded length. Therefore, the model is primarily suitable for predicting the global bond-transfer response. Future work should incorporate measured geometric imperfections, spatially varying bond–slip relationships, and more detailed damage evolution parameters to further improve the numerical description of temperature-dependent interface behavior.

Finally, although the proposed model showed satisfactory agreement with the independent Yan et al. dataset, the validation database remains limited. Additional experimental results covering broader temperature ranges and material conditions are required to further establish the general applicability of the model.

Future numerical studies should incorporate explicitly calibrated tensile and compressive damage evolution and examine variables such as PEEQ, DAMAGEC, DAMAGET, and SDEG to provide a more detailed description of temperature-dependent damage development.

Author Contributions: Conceptualization, M.Z. and Y.Y.; methodology, M.Z., Y.Y. and W.Z.; software, Y.Y.; validation, M.Z., Y.Y. and W.Z.; formal analysis, M.Z. and Y.Y.; investigation, Y.Y. and X.Y.; resources, X.Y.; data curation, Y.Y., X.L. and L.W.; writing—original draft preparation, M.Z. and Y.Y.; writing—review and editing, M.Z., W.Z., X.L., X.Y. and L.W.; visualization, Y.Y. and L.W.; supervision, M.Z.; project administration, Y.Y. All authors have read and agreed to the published version of the manuscript.

Funding: This research was funded by the Gansu Provincial Natural Science Foundation, grant number 25JRRA207.

Institutional Review Board Statement: Not applicable.

Informed Consent Statement: Not applicable.

Data Availability Statement: The data presented in this study are available in the article.

Conflicts of Interest: Author Yingjun Yang was employed by the company Gansu Road & Bridge Construction Group Co., Ltd. Authors Wenfeng Zhou and Xingtao Liu were employed by the company Gansu Wantai Construction Engineering Co., Ltd. The remaining authors declare that the research was conducted in the absence of any commercial or financial relationships that could be construed as a potential conflict of interest. The funders had no role in the design of the study; in the collection, analysis, or interpretation of data; in the writing of the manuscript; or in the decision to publish the results.

References

1. Wu, F.H.; Lv, Y.L.; Shou, Q.Y. The application of high strength/performance concrete in Chinese construction. *J. Appl. Mech. Mater.* **2013**, *357–360*, 1008–1011. [CrossRef]
2. Graybeal, B.; Brühwiler, E.; Kim, B.-S.; Toutlemonde, F.; Voo, Y.L.; Zaghi, A. International Perspective on UHPC in Bridge Engineering. *J. Bridge Eng.* **2020**, *25*, 04020094. [CrossRef]
3. Ju, Y.; Liu, H.; Chen, J.; Jia, Y.; Peng, P. Toughness and characterization of reactive powder concrete with ultra-high strength. *J. Sci. China Ser. E Technol. Sci.* **2009**, *52*, 1000–1018. [CrossRef]
4. Han, L.H. Theoretical analyses and experimental researches for the behaviors of high strength concrete filled steel tubes subjected to axial compression. *Ind. Constr.* **1997**, *27*, 39–44. (In Chinese)
5. Han, L.H. *Concrete-Filled Steel Tube Structures: Theory and Practice*, 3rd ed.; Science Press: Beijing, China, 2016. (In Chinese)
6. Wang, F.C.; Xie, W.Q.; Li, B.; Han, L.-H. Experimental study and design of bond behavior in concrete-filled steel tubes (CFST). *Eng. Struct.* **2022**, *268*, 114750. [CrossRef]
7. Han, L.-H.; Tao, Z.; Huang, H.; Zhao, X.-L. Concrete-filled double skin (SHS outer and CHS inner) steel tubular beam-columns. *Thin-Walled Struct.* **2004**, *42*, 1329–1355. [CrossRef]
8. Sheng, Z.Y. Summary of the Development on Concrete Filled Steel Tube Structure. *Appl. Mech. Mater.* **2012**, *256–259*, 670–673. [CrossRef]
9. Zhang, J.-B.; Xu, Z.-D.; Han, J.-S.; Wang, X.-D. Prediction of the Thermal Contact Resistance at the Steel-Concrete Interface of CFST Columns with Circular Cross-Section. *Mech. Adv. Mater. Struct.* **2012**, *19*, 530–542. [CrossRef]
10. Xie, J.; Yan, J.B. Experimental studies and analysis on compressive strength of normal-weight concrete at low temperatures. *Struct. Concr.* **2018**, *19*, 1235–1244. [CrossRef]
11. Huang, Y.; Yang, Z.; Fu, J.; Liu, A. Long-term lateral-torsional buckling behavior of pin-ended CFST arches under uniform radial loads and temperature field. *Mech. Adv. Mater. Struct.* **2020**, *28*, 2472–2486. [CrossRef]
12. Virdi, K.; Dowling, P.J. Bond strength in concrete filled steel tubes. *IABSE Proc.* **1980**, *4*, 125–139.
13. Roeder, C.W.; Cameron, B.; Brown, C.B. Composite action in concrete filled tubes. *J. Struct. Eng.* **1999**, *125*, 477–484. [CrossRef]
14. Xiliang, K.; Yaofang, C.; Yun, T.; Jianyang, X. Experimental study and numerical analysis of bond-slip properties of concrete-filled steel tube. *Eng. Mech.* **2010**, *27*, 102–106. (In Chinese)
15. Li, W.; Chen, B.; Han, L.-H.; Lam, D. Experimental study on the performance of steel-concrete interfaces in circular concrete-filled double skin steel tube. *Thin-Walled Struct.* **2020**, *149*, 106660. [CrossRef]
16. Tao, Z.; Han, L.-H.; Uy, B.; Chen, X. Post-fire bond between the steel tube and concrete in concrete-filled steel tubular columns. *J. Constr. Steel Res.* **2010**, *67*, 484–496. [CrossRef]
17. Song, T.-Y.; Tao, Z.; Han, L.-H.; Uy, B. Bond Behavior of Concrete-Filled Steel Tubes at Elevated Temperatures. *J. Struct. Eng.* **2017**, *143*, 04017147. [CrossRef]
18. Wei, L.; Bing, C.; Lin-Hai, H.; Packer, J.A. Pushout tests for concrete-filled double skin steel tubes after exposure to fire. *Thin-Walled Struct.* **2022**, *176*, 109274. [CrossRef]
19. Xue, L.H.; Cai, S.H. Bond strength at the interface of concrete-filled steel tube columns (Part 1). *Build. Sci.* **1996**, *12*, 22–28. (In Chinese)
20. Yan, J.-B.; Xie, W.; Zhang, L.; Lin, X.-C. Bond behaviour of concrete-filled steel tubes at the Arctic low temperatures. *Constr. Build. Mater.* **2019**, *210*, 118–131. [CrossRef]

21. Kang, X.L. Study on Mechanical Properties and Bond Slip Properties of Concrete-Filled Steel Tube Composite. Ph.D. Thesis, Xi'an University of Architecture and Technology, Xi'an, China, 2008. (In Chinese)
22. Liu, Y.X. Theoretical Analysis of the Bond Slip Property of Concrete-Filled Steel Tube and Verification by ANSYS Program. Master's Thesis, Xi'an University of Architecture and Technology, Xi'an, China, 2006. (In Chinese)
23. Hu, B.; Wang, J.G. Numerical simulation of bond slip interaction between steel tube and concrete. *China Highw. J.* **2009**, *22*, 84–91. (In Chinese) [CrossRef]
24. Wang, L.; Yang, X.J.; Li, Z.Q.; Yin, P.; Zhou, X.F.; Hu, Q. Experimental study on the interfacial bonding performance of concrete-filled steel tubes at different ambient temperatures. *Thin-Walled Struct.* **2024**, *205*, 112368. [CrossRef]
25. *GB/T 228.2-2015*; Metallic Materials—Tensile Testing—Part 2: Method of Test at Elevated Temperature. Standards Press of China: Beijing, China, 2015. (In Chinese)
26. *GB/T 228.3-2019*; Metallic Materials—Tensile Testing—Part 3: Method of Test at Low Temperature. Standards Press of China: Beijing, China, 2019. (In Chinese)
27. *GB/T 228.1-2021*; Metallic Materials—Tensile Testing—Part 1: Method of Test at Room Temperature. Standards Press of China: Beijing, China, 2021. (In Chinese)
28. *GB/T 50081-2019*; Standard for Test Method of Physical and Mechanical Properties of Concrete. China Architecture & Building Press: Beijing, China, 2019. (In Chinese)
29. *GB 51081-2015*; Technical Specification for the Application of Concrete in Low-Temperature Environments. China Association for Engineering Construction Standardization: Beijing, China, 2015. (In Chinese)
30. Lyu, W.-Q.; Han, L.-H. Investigation on bond strength between recycled aggregate concrete (RAC) and steel tube in RAC-filled steel tubes. *J. Constr. Steel Res.* **2019**, *155*, 438–459. [CrossRef]
31. Zhao, H.; Li, J.; Wang, R.; Lam, D.; Zhang, Y. Study on interfacial bond behavior of recycled aggregate concrete filled stainless steel tubes (RAC-FSST). *Constr. Build. Mater.* **2021**, *313*, 125532. [CrossRef]
32. Xu, C.; Chengkui, H.; Decheng, J.; Yuancheng, S. Push-out test of pre-stressing concrete filled circular steel tube columns by means of expansive cement. *Constr. Build. Mater.* **2007**, *23*, 491–497. [CrossRef]
33. Debnath, P.P.; Xu, F.; Chan, T.-M. Load transfer mechanism in concrete-filled steel tubular columns: Developments, challenges and opportunities. *J. Constr. Steel Res.* **2023**, *203*, 107781. [CrossRef]
34. Jiang, Z.; He, B.; Zhu, X.; Ren, Q.; Zhang, Y. State-of-the-art review on properties evolution and deterioration mechanism of concrete at cryogenic temperature. *Constr. Build. Mater.* **2020**, *257*, 119456. [CrossRef]
35. Chatterji, S. Aspects of the freezing process in a porous material–water system: Part 1. Freezing and the properties of water and ice. *Cem. Concr. Res.* **1999**, *29*, 627–630.
36. Tao, Z.; Song, T.-Y.; Uy, B.; Han, L.-H. Bond behavior in concrete-filled steel tubes. *J. Constr. Steel Res.* **2016**, *120*, 81–93. [CrossRef]
37. Xu, Y.L. Experimental Study on Bond Anchoring Performance of Deformed Rear-Concrete. Ph.D. Thesis, Tsinghua University, Beijing, China, 1990. (In Chinese)
38. Xu, K.C.; Bi, L.P.; Chen, M.C. Experimental study of interfacial bonding stress-slip constitutive relationship of concrete-filled steel tube. *J. Build. Struct.* **2015**, *36*, 407–412. (In Chinese) [CrossRef]
39. Li, X.E. Study on Interfacial Bond Property of Concrete with Round Steel Tube After Freeze-Thaw Cycle. Master's Thesis, Qingdao University of Science and Technology, Qingdao, China, 2022.
40. Han, L.H. *Concrete-Filled Steel Tube Structures: Theory and Practice*, 4th ed.; Science Press: Beijing, China, 2022.
41. Zhuo, Z.; Fan, Z.; Ling, S. *Nonlinear Finite Element Analysis and Examples of ABAQUS*; Science Press: Beijing, China, 2005; p. 548.
42. Genikomsou, A.S.; Polak, M.A. Finite element analysis of punching shear of concrete slabs using damaged plasticity model in ABAQUS. *Eng. Struct.* **2015**, *98*, 38–48. [CrossRef]
43. *GB 50010-2010*; Code for Design of Concrete Structures. China Architecture & Building Press: Beijing, China, 2010.

Disclaimer/Publisher's Note: The statements, opinions and data contained in all publications are solely those of the individual author(s) and contributor(s) and not of MDPI and/or the editor(s). MDPI and/or the editor(s) disclaim responsibility for any injury to people or property resulting from any ideas, methods, instructions or products referred to in the content.